nature COMMUNICATIONS

ARTICLE

Received 19 Jul 2014 | Accepted 21 Nov 2014 | Published 14 Jan 2015

DOI: 10.1038/ncomms6923 OPEN

Size dependence of phase transitions in aerosol nanoparticles

Yafang Cheng[1], Hang Su[1], Thomas Koop[2], Eugene Mikhailov[3] & Ulrich Pöschl[1]

Phase transitions of nanoparticles are of fundamental importance in atmospheric sciences, but current understanding is insufficient to explain observations at the nano-scale. In particular, discrepancies exist between observations and model predictions of deliquescence and efflorescence transitions and the hygroscopic growth of salt nanoparticles. Here we show that these discrepancies can be resolved by consideration of particle size effects with consistent thermodynamic data. We present a new method for the determination of water and solute activities and interfacial energies in highly supersaturated aqueous solution droplets (Differential Köhler Analysis). Our analysis reveals that particle size can strongly alter the characteristic concentration of phase separation in mixed systems, resembling the influence of temperature. Owing to similar effects, atmospheric secondary organic aerosol particles at room temperature are expected to be always liquid at diameters below ~20 nm. We thus propose and demonstrate that particle size should be included as an additional dimension in the equilibrium phase diagram of aerosol nanoparticles.

[1] Multiphase Chemistry Department, Max Planck Institute for Chemistry, 55128 Mainz, Germany. [2] Faculty of Chemistry, Bielefeld University, 33615 Bielefeld, Germany. [3] Institute of Physics, St. Petersburg State University, 198904 St. Petersburg, Russia. Correspondence and requests for materials should be addressed to H.S. (email: h.su@mpic.de) or to Y.C. (email: yafang.cheng@mpic.de) or to U.P. (email: u.poschl@mpic.de).

The phase state of aerosol particles is a key determinant of their physico-chemical interactions, climate and health effects[1–4]. Chemical composition, relative humidity and temperature have been recognized as the main factors controlling aerosol phase state[1,2,5], but they are insufficient to explain observations for nanometer-sized particles, even for well-studied inorganic reference substances[3,6–10], such as ammonium sulphate (AS).

Progress in resolving these discrepancies has been hampered by a lack of reliable thermodynamic data, such as water and solute activities and interfacial energies. This lack of data exists because nanodroplets can become more highly supersaturated (with respect to a crystal) when compared with bulk solution samples, but traditional measurement techniques and data, especially the liquid-vapour interfacial energy (σ_{lv}, also called surface tension), are mostly limited to sub-saturated and saturated solutions. The existing measurement techniques for σ_{lv} often require touching the solution by needles or other intermediates, such as a plate or capillary tube[11]. Solute crystallization induced by heterogeneous nucleation can take place in supersaturated solution on the contact surface, which makes the precise measurements difficult. Measurement of σ_{lv} using the vibration modes of a magnetically levitated drop could avoid the contact but is limited to supermicrometre particles owning to the stability in the magnetic trap[12]. Measurements of water activities (a_w) have been extended to supersaturated range by Electrodynamic Balance (EDB) methods[13,14] (for example, up to $\sim 30\,mol\,kg^{-1}$ for AS), but it is not applicable for the nanosize range either.

To overcome these limitations, we develop a new method for the determination of these specific thermodynamic parameters, closing the gap between experimental and modelled results. Further analysis reveals that particle size can strongly alter the phase separation process in mixed systems. We thus propose and demonstrate that particle size should be included as an additional dimension in the equilibrium phase diagram of aerosol nanoparticles.

Results

Thermodynamic properties of supersaturated nanodroplets. According to theoretical predictions, AS nanoparticles are expected to show a strong size dependence of deliquescence relative humidity (DRH) similar to sodium chloride (NaCl), with differences up to ~10% RH between particles with dry diameters of 6 and 60 nm (refs 6,8; Fig. 1a). Experimental data, however, reveal a much weaker size dependence for AS, that is, similar DRH values for 6-nm and 60-nm particles[9] (Fig. 1b). Moreover, model calculations based on previously available thermodynamic data agree reasonably well with the hygroscopic growth observed for both 60-nm and 6-nm NaCl particles and also for 60-nm AS particles, but deviate strongly for 6-nm AS particles as shown in Fig. 1a,b. Further investigations of these discrepancies, however, were impeded by a lack of reliable thermodynamic data.

In this study, a new method, termed Differential Köhler Analysis (DKA), is developed for the determination of thermodynamic properties from hygroscopic growth measurement data of aerosolized nanodroplets. Differential application of the classical Köhler equation to aerosol particles with the same hygroscopic growth factor but different dry diameters enables the simultaneous determination of a_w and σ_{lv} as a function of solute concentration (see Methods and Supplementary Note 1). By applying the DKA approach to high precision measurement data from hygroscopic tandem differential mobility analyser (HTDMA) experiments[9] (see Methods), we obtained consistent and robust estimates for a_w and σ_{lv} of aqueous AS nanoparticles with molalities up to $b \sim 160\,mol\,kg^{-1}$ (solute mass fractions up to $x_s \sim 0.96$) (Fig. 2). The DKA results agree well with literature data in the previously accessible range of concentrations and enable accurate model calculations of the hygroscopic growth of highly concentrated AS nanoparticles (purple line in Fig. 1b); for DKA results of NaCl nanoparticles see Supplementary Fig. 1.

Measured and predicted phase transitions and equilibria. For model predictions of the DRH and ERH (efflorescence relative humidity), we calculated solute activity (a_s) and obtained the interfacial energy of the salt in its saturated aqueous solution upon deliquescence (σ_{sl}) and the interfacial energy of salt embryos (γ_{sl}) in highly supersaturated aqueous solution upon efflorescence based on the DKA-derived a_w and σ_{lv} (Supplementary Notes 2,3). With this approach, we are able to determine σ_{sl} and γ_{sl} at one particular diameter and then apply them for predictions over the entire size range of 6–60 nm (see Methods). As shown in Fig. 1c,d, the DKA-based thermodynamic data allow quantifying and reconciling the contrasting size dependencies in the relative humidity thresholds of the deliquescence and efflorescence transitions for both AS and NaCl nanoparticles. The experimental DRH values observed for NaCl and AS nanoparticles are in a good agreement with our Köhler-Ostwald-Freundlich model[15] using DKA data (solid lines in Fig. 1c) but not with the modelling approach neglecting the effect of particle size on solubility (dashed lines in Fig. 1c). The solute molality on deliquescence (b^*) represents the size-dependent water solubility of nanoparticles. It is much higher than the solubility of bulk material (b_{bulk}^*) and agrees well with the Ostwald-Freundlich model prediction (Fig. 1e). Owing to a lack of reliable a_s and σ_{sl} data, previous studies failed to reproduce the size-dependent solubility of AS, and therefore, were not able to explain the different size dependence of DRH for AS and NaCl[6,7].

The observed ERH values also agree very well with our predictions using DKA data (Fig. 1d) in a model combining the Köhler equation and classical nucleation theory[16,17] (see Methods). The solute molality upon efflorescence (b_e) represents the threshold concentration triggering solute nucleation and liquid–solid phase separation. It is not sensitive to particle size for NaCl, where a 30% increase in b_e was sufficient to maintain the same nucleation rate despite a 1,000-fold volume reduction between 60-nm and 6-nm particles (Fig. 3a and red diamonds in Fig. 1f). In contrast, an about 12-fold increase in b_e was required to trigger the nucleation and phase separation when going from 60-nm to 6-nm AS particles (Fig. 3b and blue circles in Fig. 1f). The different behaviour of NaCl and AS can be attributed largely to different relations between solute activity and concentration, that is, for the same change of activity, a stronger increase in molality is required for AS than for NaCl (Supplementary Fig. 2).

It has been shown that water activity rather than molality is the determinant for the homogenous nucleation of ice in solutions[18]. Similarly, our results demonstrate that solute nucleation and phase separation are determined by solute activity, implying that the non-ideality of solution properties become vital for the calculation of nucleation rates and understanding of phase transitions, especially for nanodroplets (Fig. 3). Indeed, the weaker size dependence of the threshold relative humidity (DRH, ERH) of AS is a consequence of its stronger size dependence of the threshold solute concentration (b^*, b_e) compared with NaCl (Supplementary Fig. 3).

The existence of metastable AS droplets with molalities up to $\sim 380\,mol\,kg^{-1}$ (AS:H_2O molar ratio ~7:1) upon efflorescence (Fig. 1f) provides new insight on the phase state of salt nanoparticles. Such a high solute-to-solvent ratio implies that the droplet is no longer a typical aqueous solution, but may be regarded as a 'molten' salt particle with a few water molecules as a

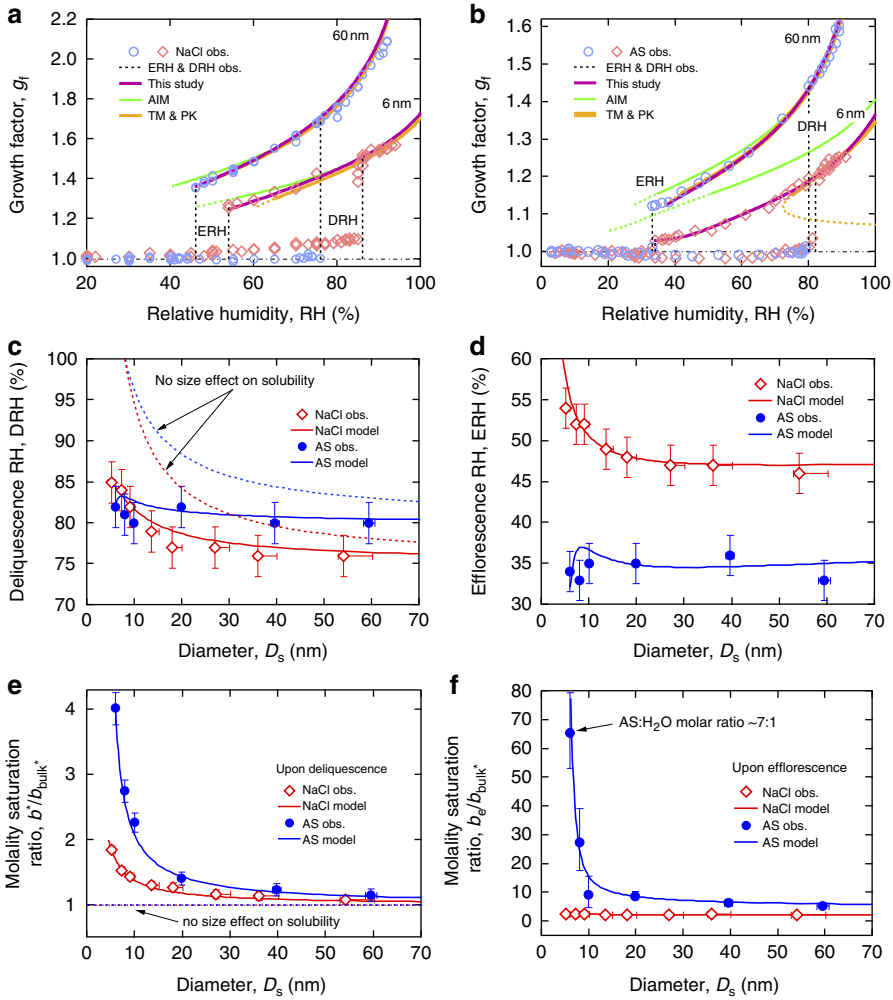

Figure 1 | Hygroscopic growth, deliquescence and efflorescence of nanoparticles. (**a**,**b**) Hygroscopic growth curves of sodium chloride (NaCl) and ammonium sulphate (AS). Growth factor data are taken from HTDMA experiments[8,9] for particles with dry diameters of 60 nm (blue circle) and 6 nm (red diamond). Köhler model curves are based on different thermodynamic data sets: in this study, purple line with DKA (Differential Köhler Analysis) derived data for AS and modified TM & SP (Tang-Munkelwitz[35,36] and Seinfeld-Pandis[37]) for NaCl; AIM (Aerosol Inorganics Model[38]), green line; TM & PK (Tang-Munkelwitz[35,36] and Pruppacher-Klett[39]) as in Biskos *et al.*[8,9], orange line (Supplementary Note 3). Dashed lines indicate extrapolation beyond validated concentration range. Size-dependent threshold values of relative humidity and solute saturation ratio on deliquescence (**c**,**e**) and efflorescence (**d**,**f**). Saturation ratios refer to bulk water solubility expressed in solute molality (b_{bulk}^*). Model curves were obtained by combination of the Köhler equation with the Ostwald–Freundlich equation for deliquescence and with classical nucleation theory for efflorescence. Dashed lines indicate model predictions without consideration of size-dependent solubility. Error bars are estimated by considering measurement uncertainties.

'solute' or 'impurity' (here 'molten' does not imply a high melting point). By further reducing particle size, we expect an increase in the AS mole fraction, such that the particle ultimately becomes a pure molten salt at ambient temperature. This is also supported by the fact that the interfacial energy σ_{lv} retrieved here at a temperature $T = 298\,K$ approaches a value of $0.182\,N\,m^{-1}$ (Fig. 2b), which is consistent with the value of $0.185\,N\,m^{-1}$ predicted for a molten AS at the same temperature[19].

Size effects on phase transitions. Although the Kelvin effect is commonly considered for liquid-vapour equilibrium and phase partitioning, size effects on the liquid-solid equilibrium upon phase transitions have been rarely taken into account in atmospheric thermodynamic and kinetic models. On the basis of the above results, we propose to include the particle dry diameter (D_s) as the third dimension in the liquid–solid equilibrium phase diagrams of aerosol particles. Figure 4a shows such a 3-D phase diagram for the AS-water system. In Fig. 4a, the surfaces represent the equilibrium between liquid and crystalline phases. It is estimated from polynomial fitting to literature data (solid circles). A slice on the surface at $D_s^{-1} = 0$ ($D_s \to \infty$) equals the traditional T-x_s diagram for bulk material as illustrated in Fig. 4b.

A slice on the surface at constant T provides a D_s^{-1}-x_s phase diagram showing the influence of particle size on equilibrium composition. As an example, Fig. 4c shows a D_s^{-1}-x_s slice at 215 K, which exhibits a similar pattern as the traditional T-x_s diagram in Fig. 4b. Figure 4d displays the D_s^{-1}-x_s diagram at 298 K, which contains the observed size-dependent solubility of AS particles reflecting the Ostwald–Freundlich effect[15]. Note that, at this temperature, the ice phase does not exist. Extrapolation of the experimental data for aqueous AS to $x_s = 1$ leads to a critical melting diameter of ~4 nm, that is, pure AS particles below this size are expected to be in a liquid state at 298 K.

Finally, a slice at constant x_s gives a T-D_s^{-1} phase diagram showing the effect of particle size on phase transition temperature (Fig. 4e). For example, in a system with an AS mass fraction of $x_s = 0.63$, the characteristic temperature for complete dissolution

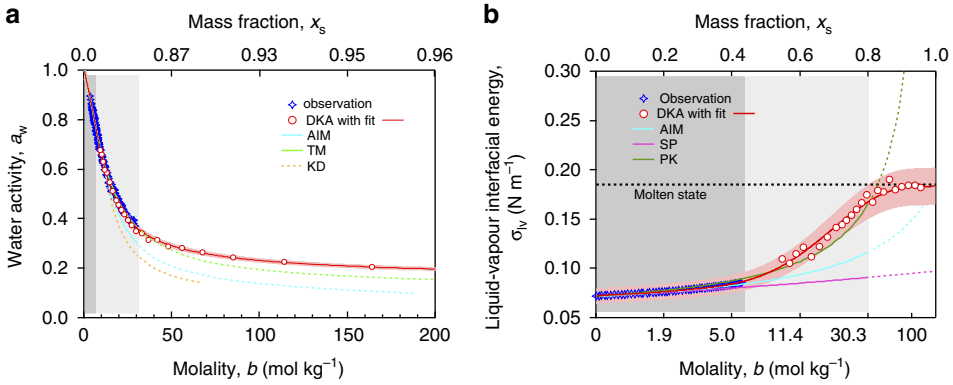

Figure 2 | Concentration-dependent thermodynamic properties of ammonium sulphate solution. (**a**,**b**) Water activity (a_w, on a mole fraction basis) and liquid-vapour interfacial energy (σ_{lv}) are plotted against solute molality (b) and mass fraction (x_s). The DKA-derived a_w and σ_{lv} (red open circles) are compared with observations (blue stars)[39,40], AIM (Aerosol Inorganic Model[38], blue line), and other parameterizations for a_w (TM = Tang-Munkelwitz[35], green line; KD = Kreidenweis[41], orange line) and σ_{lv} (PK = Pruppacher-Klett[39], dark green line; SP = Seinfeld-Pandis[37], purple line) (Supplementary Note 3). Dashed lines indicate extrapolation beyond validated concentration range. The equations for the best fit of DKA results (red lines) can be found in Supplementary Table 1. Red shaded areas indicate the uncertainties in the DKA retrieval, estimated by Monte Carlo analyses (Supplementary Note 1). The dark and light grey shaded areas mark the sub-saturated and saturated concentration with respect to bulk solution and supersaturated concentration before efflorescence of supermicrometre droplets, respectively. The white area marks the highly supersaturated concentration where the a_w data are not available in the literature.

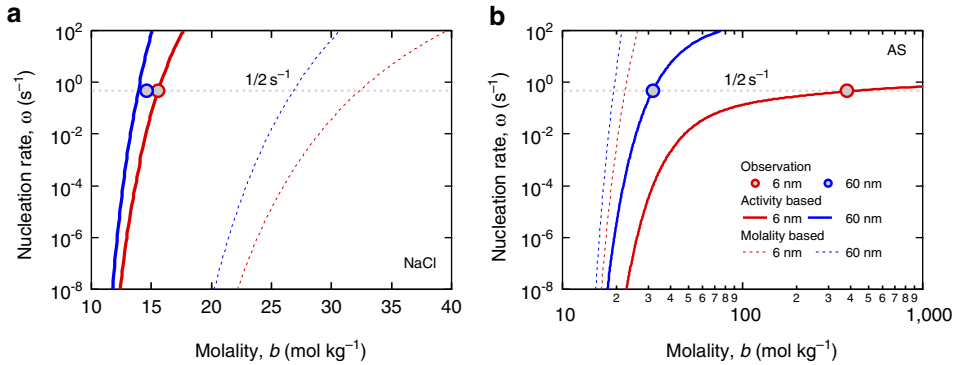

Figure 3 | Homogeneous nucleation rate as a function of solute molality. (**a**) Sodium chloride (NaCl) and (**b**) ammonium sulphate (AS). The nucleation rates (ω) are calculated from solute activity (thick lines) and concentration (thin dashed lines) at selected particle sizes (6 and 60 nm). Grey dashed line corresponds to ω of 0.5 s^{-1}, at which at least one nucleation event is triggered during the expected induction time interval (t_i and $\omega t_i = 1$). Here, t_i is estimated as 2 s according to the residence time in the HTDMA experiments[9]. The circles represent the observed nucleation (efflorescence) concentrations.

decreases from ~470 K for bulk material to ~298 K for 10-nm particles. At $x_s = 0$ or 1, the diagram becomes a T-D_s^{-1} diagram for a pure substance, reflecting the Gibbs–Thomson effect[20]. Related effects of particle size on melting, freezing and glass transitions have been reported and quantified for a wide range of materials such as water, organic compounds and metals[21–23] (Supplementary Fig. 4). Our results demonstrate that similar effects and formalisms also apply to other phase transition processes and mixed systems, such as liquid–solid phase separation in salt-water droplets. The size-dependent phase transition temperature and increased solubility of nanoparticles reflect a tendency of smaller particles for staying in liquid and mixed phase compared with bulk materials (Supplementary Fig. 5). This may partly explain the unresolved size-dependent morphology of organic-AS particles, that is, smaller particles are internally mixed while larger particles adopt a de-mixed partially engulfed structure[10].

Discussion

According to the size effects outlined above, aerosol particles of identical chemical composition may coexist in different states in the atmosphere depending on particle diameter. Thus, we are interested in the critical diameter ($D_{s,c}$) below which aerosol particles are expected to be liquid and well-mixed at ambient temperature. Using T-D_s^{-1} diagrams like Fig. 4e for particles with different chemical composition (Supplementary Fig. 6), we obtained critical dry diameters as a function of bulk phase transition temperature (T_{bulk}). As shown in Fig. 5, all data for aqueous AS and NaCl particles available at 298 K converge onto a compact near-linear correlation of $1/D_{s,c}$ versus T_{bulk}. The glass transition of low chain length polystyrene[22] as the only organic reference material (with low molecular weight) for which similar substrate-free data are currently available falls onto the same correlation line. These findings suggest that the influence of particle size on the liquefaction of substances is related to bulk phase transition temperature in a similar way for different salts as well as organic compounds, implying a close relationship between interfacial energy and the enthalpy of phase transition similar to the Turnbull relation[24] (see Supplementary Fig. 7 and Supplementary Discussion for more details).

Chamber experiments with pine emissions-derived secondary organic aerosol (SOA) as well as field measurements of

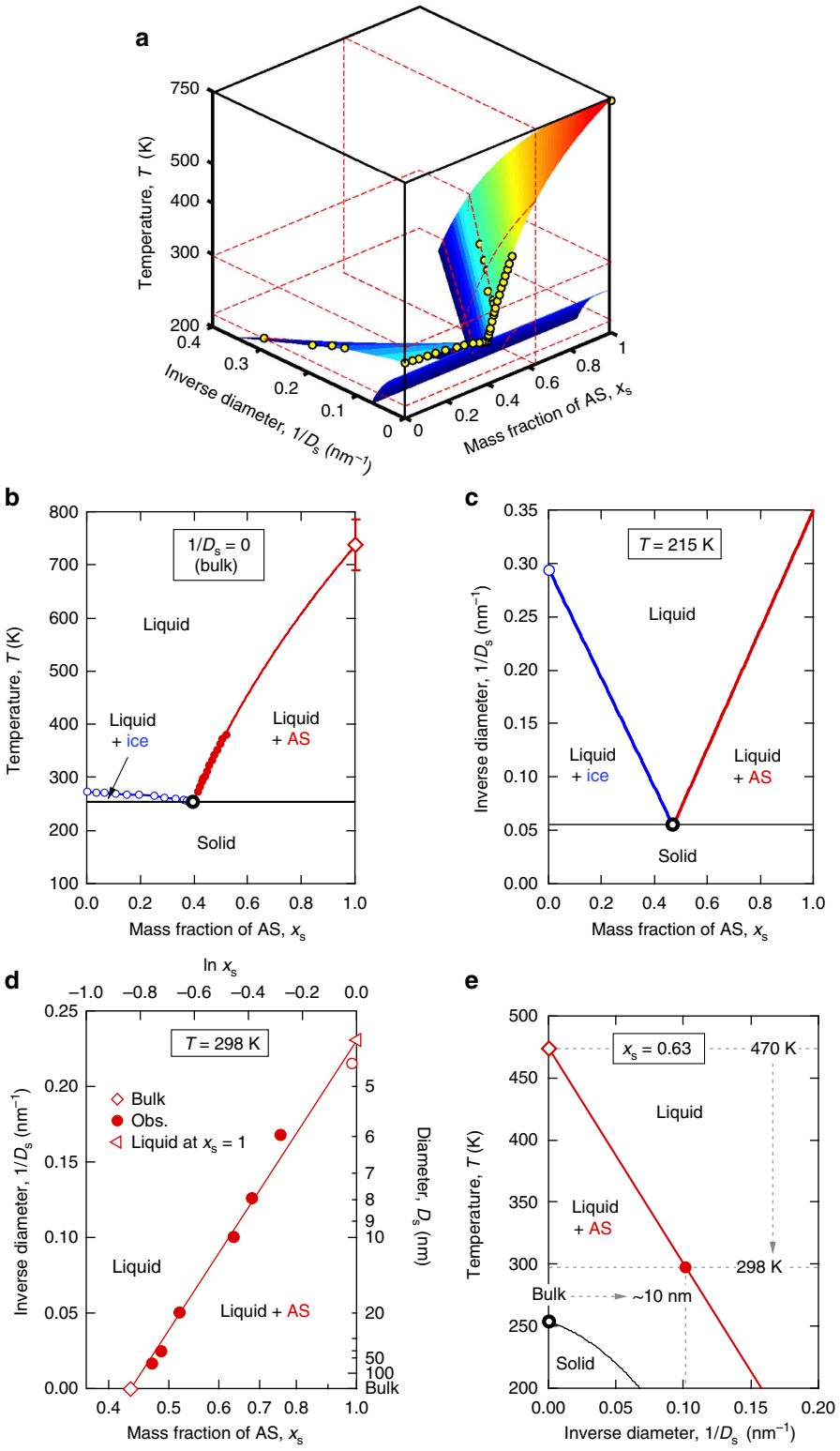

Figure 4 | Liquid–solid equilibrium phase diagrams for the ammonium sulphate—water system. (**a**) 3D phase diagrams in the coordinates of inverse diameter $1/D_s$, temperature T and ammonium sulphate (AS) mass fraction x_s. The solid circles represent the available data of bulk phase diagram of aqueous AS solution[42], size-dependent melting temperature of ice[23] and solubility of AS. The surfaces, coloured by the corresponding temperature, are estimated from polynomial fitting, showing the equilibrium between liquid and crystalline phases. The dashed planes illustrate the following slices. (**b**) The T-x_s phase diagram for bulk solution. The temperature-dependent phase separation of aqueous AS bulk solution (red line) is constrained by the melting temperature of AS at $x_s = 1$ (open diamond). The error bar shows the uncertainty of AS melting temperature according to close-cell measurements[43]. The D_s^{-1}-x_s phase diagram at 215 K (**c**) and at 298 K (**d**). In (**d**), the solid circles represent the observations for nano-sized droplets. The open diamond is the bulk solubility and the open circle is predicted by the DKA-constrained solute activity. The critical melting diameter (open triangle) is obtained by linear extrapolation to $x_s = 1$ (molten state). (**e**) The T-D_s^{-1} phase diagram at $x_s = 0.63$. The black open circle represents the eutectic point for bulk solution (also in **b** and **c**). The black line shows the size dependence of eutectic points.

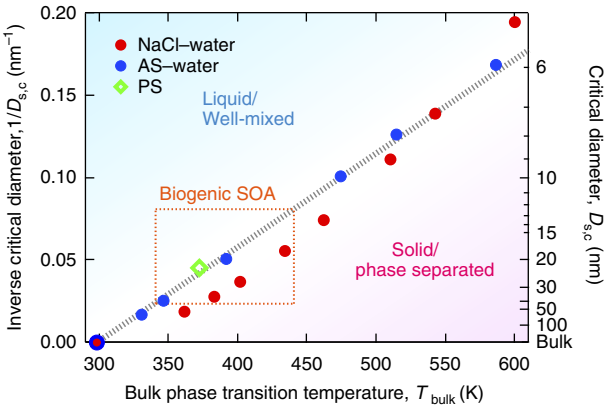

Figure 5 | Dependence of critical diameter on bulk phase transition temperature. Inverse critical diameters of liquefaction at 298 K ($D_{s,c}^{-1}$) are plotted against bulk phase transition temperatures (T_{bulk}) for aqueous ammonium sulphate (AS, blue solid circle), aqueous sodium chloride (NaCl, red solid circle) and low chain length polystyrene (PS, green open diamond)[22]. The data points are observations and the dotted line is a linear fit to all data through the point of [298 K, $D_s^{-1}=0$]. The orange dashed line bounded area indicates the parameter range estimated for atmospheric biogenic secondary organic aerosol (SOA).

atmospheric biogenic SOA indicate a change of particle phase state at ~20–30 nm (refs 3,25), suggesting that particles below this limit are in the liquid-like state. This observation appears consistent with a critical diameter around ~20 nm (12–40 nm), which can be derived from the estimated bulk melting temperatures of individual functionalized acids found in biogenic SOA (~340–440 K, orange dashed line bounded area in Fig. 5, see Supplementary Note 4)[2]. This consistency increases confidence in the similarity of T_{bulk}-$D_{s,c}$ relations. SOA particles usually consist of mixtures of multiple compounds, which reduces the bulk melting temperature[26], thus increasing the critical diameter and implying that SOA particles in the nucleation mode are very likely always liquid (of potentially high viscosity). The liquid-to-solid transition of SOA particles observed at ~20–30 nm was suggested to be a glass transition[3,25], for which the transition temperature is usually by a factor of ~0.7 lower than for melting[2]. Explaining the observed transition would thus require a fairly high bulk glass transition temperature (~370 K), suggesting that the SOA particles may contain oligomers or polymers, in agreement with independent observations[27].

The methods and results presented in this study advance the understanding and challenge the traditional modelling of atmospheric aerosol phase state and processing. The size effects on the phase states may have important implications for a number of atmospheric interfacial and condensed phase processes such as nucleation, water/gas uptake, polymerization and heterogeneous reactions[2,27–29]. The combination of the DKA method and tandem differential mobility analyser technique can be used to study the thermodynamic properties of nanoparticles from a wide range of materials and enables substrate-free experimental investigation of nanoparticles not only on humidification and drying but also with regard to other types of conditioning, for example, exposure to organic solvents, heat treatment and volatilization[30,31]. Thus, the scientific approach presented here may be useful for nanoparticle studies in various fields, including the environmental, biomedical and materials sciences[20,32].

Methods

HTDMA experiments. Our analysis is based on the Harvard hygroscopic tandem differential mobility analyser (HTDMA) measurements[8,9], where a mono-disperse dry particle fraction of dry diameter D_s is selected by the first DMA, equilibrated to a defined relative humidity (equivalent to water vapour saturation ratio s_w = RH/100%) and finally goes through a second DMA for the determination of the humidified size distribution. The HTDMA results were usually reported in the form of the growth factor g_f as a function of s_w at each D_s. Details of shape factor correction of HTDMA data can be found in Supplementary Note 1. Data from the efflorescence mode experiments (containing the most concentrated droplet solutions) are adopted for the DKA analysis.

Differential Köhler analysis (DKA). The theoretical basis of the DKA method is the Köhler equation[33], which describes the equilibrium s_w over a spherical droplet as a function of a_w, σ_{lv} and the droplet size D_{sol}

$$s_w = a_w \exp\left(\frac{4\sigma_{lv}v_w}{RTD_{sol}}\right) = a_w \exp\left(\frac{4\sigma_{lv}v_w}{RTD_s g_f}\right) \quad (1)$$

where v_w is the partial molar volume of water (Supplementary Note 1), R is the universal gas constant and T is temperature. D_{sol} in equation (1) is often replaced by the product of D_s and g_f, in which D_s is the dry diameter of spherical solute particles and g_f is the particle geometrical diameter growth factor, that is, $g_f = D_{sol}/D_s$. As parameters s_w, D_s and g_f can be determined from the HTDMA measurements, σ_{lv} and a_w (considered as size-independent) become the only unknowns in equation (1). Note that σ_{lv} and a_w are both functions of g_f (g_f represents the solute concentration x_s, see Supplementary Note 1). For each x_s (or g_f), we need to construct at least two independent equations by performing HTDMA measurements at different D_s to realize the differential analysis as follows. Converting equation (1) into logarithmic form, we have

$$\ln s_w = \ln a_w(g_f) + \frac{A}{D_s}\sigma_{lv}(g_f) \quad (2)$$

where $A = 4v_w/(RTg_f)$. With measurements at two dry diameters D_{s1} and D_{s2}, we have

$$a_w = \frac{S_{w1}^{\left(\frac{D_{s1}}{D_{s1}-D_{s2}}\right)}}{S_{w2}^{\left(\frac{D_{s2}}{D_{s1}-D_{s2}}\right)}} \quad \text{and} \quad \sigma_{lv} = \left(\frac{A}{D_{s1}} - \frac{A}{D_{s2}}\right)^{-1}(\ln s_{w1} - \ln s_{w2}) \quad (3)$$

where s_{w1} and s_{w2} are measured at the same g_f but at D_{s1} and D_{s2}, respectively. When measurements at the same g_f are available for more than two initial particle dry diameters, a multiple regression was applied to all sizes resulting in a best estimate of a_w and σ_{lv}. More details about the DKA method can be found in Supplementary Note 1.

Modelling of deliquescence and efflorescence. Deliquescence of salt particle of dry diameter D_s happens when the ambient s_w equals the equilibrium s_w over a droplet of the wet diameter equal to D_s, and saturated with respect to crystalline salt particles of size D_s. The deliquescence concentration b^* was determined by the Ostwald–Freudlich equation[15] through corresponding deliquescence solute activity a_s^*

$$a_s^* = a_{s,bulk}^* \exp\frac{4\sigma_{sl}M_s}{m_i\rho_s RTD_s} \quad (4)$$

in which a_s^* is the solute activity in a solution saturated with respect to salt particles of diameter D_s, $a_{s,bulk}^*$ is the solute activity in saturated bulk solution, M_s is molar weight of solute, ρ_s is the density of solute and m_i is the stoichiometric number of dissociated ions. The σ_{sl} is determined to be 0.156 and 0.265 N m^{-1} for AS and NaCl, respectively (Supplementary Note 2). Substituting b^* into the Köhler equation (1) gives the DRH.

The efflorescence is predicted based on classical nucleation theory[16,17,34] along with the Köhler equation[33]. Given a Köhler curve, the volume of the droplet V_{sol} and corresponding b at each point can be easily determined. Then we can calculate the nucleation rate ω at each point by[16]

$$\omega = JV_{sol} = V_{sol}K \exp\left(-\frac{4\left(\sum_j k_j\right)\alpha^2\gamma_{sl}^3}{27\Delta G_v^2 k_b T}\right) \quad (5)$$

where V_{sol} is the volume of the droplet, K is the pre-exponential factor, k_j and α are geometrical constants dependent on the morphology of the particular crystal, ΔG_v is the excess free energy of solute per unit volume in the crystalline phase over that in solution, k_b is the Boltzmann constant. We assumed that the formation of a single critical-sized nucleus is sufficient to initiate the crystallization of the entire droplet and trigger the efflorescence. Then ERH and b_e can be determined from the point where $\omega t_i = 1$ ($t_i = 2$ s is the induction time interval for the investigated system[9]) (Fig. 3). We performed model predictions of DRH and ERH over the entire size range of 6–60 nm for AS and NaCl by this approach with σ_{sl} and γ_{sl} determined at one particular diameter (6 nm, Supplementary Note 2).

References

1. Martin, S. T. Phase transitions of aqueous atmospheric particles. *Chem. Rev.* **100,** 3403–3454 (2000).
2. Koop, T., Bookhold, J., Shiraiwa, M. & Poschl, U. Glass transition and phase state of organic compounds: dependency on molecular properties and implications for secondary organic aerosols in the atmosphere. *Phys. Chem. Chem. Phys.* **13,** 19238–19255 (2011).
3. Virtanen, A. *et al.* An amorphous solid state of biogenic secondary organic aerosol particles. *Nature* **467,** 824–827 (2010).
4. Pöschl, U. Atmospheric aerosols: composition, transformation, climate and health effects. *Angew. Chem. Int. Ed.* **44,** 7520–7540 (2005).
5. Krieger, U. K., Marcolli, C. & Reid, J. P. Exploring the complexity of aerosol particle properties and processes using single particle techniques. *Chem. Soc. Rev.* **41,** 6631–6662 (2012).
6. Russell, L. M. & Ming, Y. Deliquescence of small particles. *J. Chem. Phys.* **116,** 311–321 (2002).
7. Orr, Jr C., Hurd, F. K. & Corbett, W. J. Aerosol size and relative humidity. *J. Colloid Sci.* **13,** 472–482 (1958).
8. Biskos, G., Russell, L. M., Buseck, P. R. & Martin, S. T. Nanosize effect on the hygroscopic growth factor of aerosol particles. *Geophys. Res. Lett.* **33,** L07801 (2006).
9. Biskos, G., Paulsen, D., Russell, L. M., Buseck, P. R. & Martin, S. T. Prompt deliquescence and efflorescence of aerosol nanoparticles. *Atmos. Chem. Phys.* **6,** 4633–4642 (2006).
10. Veghte, D. P., Altaf, M. B. & Freedman, M. A. Size dependence of the structure of organic aerosol. *J. Am. Chem. Soc.* **135,** 16046–16049 (2013).
11. Damson, A. W. & Gast, A. P. *Physical Chemistry of Surfaces*, 6th edn (John Wiley & Sons, Inc., 1997).
12. Vicente, C., Yao, W., Maris, H. J. & Seidel, G. M. Surface tension of liquid ^{4}He as measured using the vibration modes of a levitated drop. *Phys. Rev. B* **66,** 214504 (2002).
13. Tang, I. N., Munkelwitz, H. R. & Wang, N. Water activity measurements with single suspended droplets: The NaCl-H_2O and KCl-H_2O systems. *J. Colloid Interf. Sci.* **114,** 409–415 (1986).
14. Chan, C. K., Liang, Z., Zheng, J., Clegg, S. L. & Brimblecombe, P. Thermodynamic properties of aqueous aerosols to high supersaturation: I-measurements of water activity of the system $Na^+ - Cl^- - NO_3^- - SO_4^{2-} - H_2O$ at ~298.15K. *Aerosol Sci. Tech.* **27,** 324–344 (1997).
15. Ostwald, W. Über die vermeintliche isomerie des roten und gelben Quecksilbersoxyds und die Oberflächenspannung fester Körper. *Z. Phys. Chem.* **34,** 495–503 (1900).
16. Cohen, M. D., Flagan, R. C. & Seinfeld, J. H. Studies of concentrated electrolyte solutions using the electrodynamic balance. 3. Solute nucleation. *J. Phys. Chem.* **91,** 4583–4590 (1987).
17. Gao, Y., Chen, S. B. & Yu, L. E. Efflorescence relative humidity of airborne sodium chloride particles: A theoretical investigation. *Atmos. Environ.* **41,** 2019–2023 (2007).
18. Koop, T., Luo, B., Tsias, A. & Peter, T. Water activity as the determinant for homogeneous ice nucleation in aqueous solutions. *Nature* **406,** 611–614 (2000).
19. Dutcher, C. S., Wexler, A. S. & Clegg, S. L. Surface tensions of inorganic multicomponent aqueous electrolyte solutions and melts. *J. Phys. Chem. A* **114,** 12216–12230 (2010).
20. Alcoutlabi, M. & McKenna, G. B. Effects of confinement on material behaviour at the nanometre size scale.. *J. Phys.: Condens. Matter* **17,** R461 (2005).
21. Couchman, P. R. & Jesser, W. A. Thermodynamic theory of size dependence of melting temperature in metals. *Nature* **269,** 481–483 (1977).
22. Forrest, J. A. & Mattsson, J. Reductions of the glass transition temperature in thin polymer films: Probing the length scale of cooperative dynamics. *Phys. Rev. E* **61,** R53–R56 (2000).
23. Pan, D., Liu, L.-M., Slater, B., Michaelides, A. & Wang, E. Melting the ice: on the relation between melting temperature and size for nanoscale ice crystals. *ACS Nano* **5,** 4562–4569 (2011).
24. Turnbull, D. Formation of crystal nuclei in liquid metals. *J. Appl. Phys.* **21,** 1022–1028 (1950).
25. Virtanen, A. *et al.* Bounce behavior of freshly nucleated biogenic secondary organic aerosol particles. *Atmos. Chem. Phys.* **11,** 8759–8766 (2011).
26. Marcolli, C., Luo, B. & Peter, T. Mixing of the organic aerosol fractions: liquids as the thermodynamically stable phases. *J. Phys. Chem. A* **108,** 2216–2224 (2004).
27. Kalberer, M. *et al.* Identification of polymers as major components of atmospheric organic aerosols. *Science* **303,** 1659–1662 (2004).
28. Murray, B. J. *et al.* Heterogeneous nucleation of ice particles on glassy aerosols under cirrus conditions. *Nat. Geosci.* **3,** 233–237 (2010).
29. Shiraiwa, M., Ammann, M., Koop, T. & Poschl, U. Gas uptake and chemical aging of semisolid organic aerosol particles. *Proc. Natl Acad. Sci. USA* **108,** 11003–11008 (2011).
30. Joutsensaari, J., Vaattovaara, P., Vesterinen, M., Hämeri, K. & Laaksonen, A. A novel tandem differential mobility analyzer with organic vapor treatment of aerosol particles. *Atmos. Chem. Phys.* **1,** 51–60 (2001).
31. Cheng, Y. F. *et al.* Size-resolved measurement of the mixing state of soot in the megacity Beijing, China: diurnal cycle, aging and parameterization. *Atmos. Chem. Phys.* **12,** 4477–4491 (2012).
32. Rabinow, B. E. Nanosuspensions in drug delivery. *Nat. Rev. Drug Discov.* **3,** 785–796 (2004).
33. Köhler, H. The nucleus in and the growth of hygroscopic droplets. *Trans. Faraday Soc.* **32,** 1152–1161 (1936).
34. Gao, Y., Chen, S. B. & Yu, L. E. Efflorescence relative humidity for ammonium sulfate particles. *J. Phys. Chem. A* **110,** 7602–7608 (2006).
35. Tang, I. N. & Munkelwitz, H. R. Water activities, densities, and refractive indices of aqueous sulfates and sodium nitrate droplets of atmospheric importance. *J. Geophys. Res-Atmos.* **99,** 18801–18808 (1994).
36. Tang, I. N. Chemical and size effects of hygroscopic aerosols on light scattering coefficients. *J. Geophys. Res-Atmos.* **101,** 19245–19250 (1996).
37. Seinfeld, J. H. & Pandis, S. N. *Atmospheric Chemistry and Physics, from Air Pollution to Climate Change* (John Wiley, 2006).
38. Clegg, S. L., Brimblecombe, P. & Wexler, A. S. Thermodynamic Model of the System $H^+ - NH_4^+ - Na^+ - SO_4^{2-} - NO_3^- - Cl^- - H_2O$ at 298.15K. *J. Phys. Chem. A* **102,** 2155–2171 (1998).
39. Pruppacher, H. R. & Klett, J. D. *Microphysics of clouds and precipitation* (Kluwer Academic Publishers, 1997).
40. Clegg, S. L., Ho, S. S., Chan, C. K. & Brimblecombe, P. Thermodynamic properties of aqueous $(NH_4)_2SO_4$ to high supersaturation as a function of temperature. *J. Chem. Eng. Data* **40,** 1079–1090 (1995).
41. Kreidenweis, S. M. *et al.* Water activity and activation diameters from hygroscopicity data-Part I: Theory and application to inorganic salts. *Atmos. Chem. Phys.* **5,** 1357–1370 (2005).
42. Xu, J., Imre, D., McGraw, R. & Tang, I. Ammonium sulfate: equilibrium and metastability phase diagrams from 40 to −50°C. *J. Phys. Chem. B* **102,** 7462–7469 (1998).
43. Kendall, J. & Davidson, A. W. The melting point of ammonium sulfate. *J. Ind. Eng. Chem.* **13,** 303–304 (1921).

Acknowledgements

This study was supported by the Max Planck Society (MPG), National Natural Science Foundation of China (41330635), the EU project PEGASOS (265148), Russian Foundation for Basic research (12-05-00620-à), and RC 'Geomodel' of St Petersburg State University.

Author contributions

Y.C. and H.S. designed and performed the study. T.K., E.M. and U.P. discussed the results, interpretation and implications and commented on the manuscript at all stages. Y.C. and H.S. wrote the supplement. Y.C., H.S. and U.P. wrote the manuscript with inputs from all the co-authors.

Additional information

Supplementary Information accompanies this paper at http://www.nature.com/naturecommunications

Competing financial interests: The authors declare no competing financial interests.

Reprints and permission information is available online at http://npg.nature.com/reprintsandpermissions/

How to cite this article: Cheng, Y. *et al.* Size dependence of phase transitions in aerosol nanoparticles. *Nat. Commun.* 6:5923 doi: 10.1038/ncomms6923 (2015).

Supplementary Figures

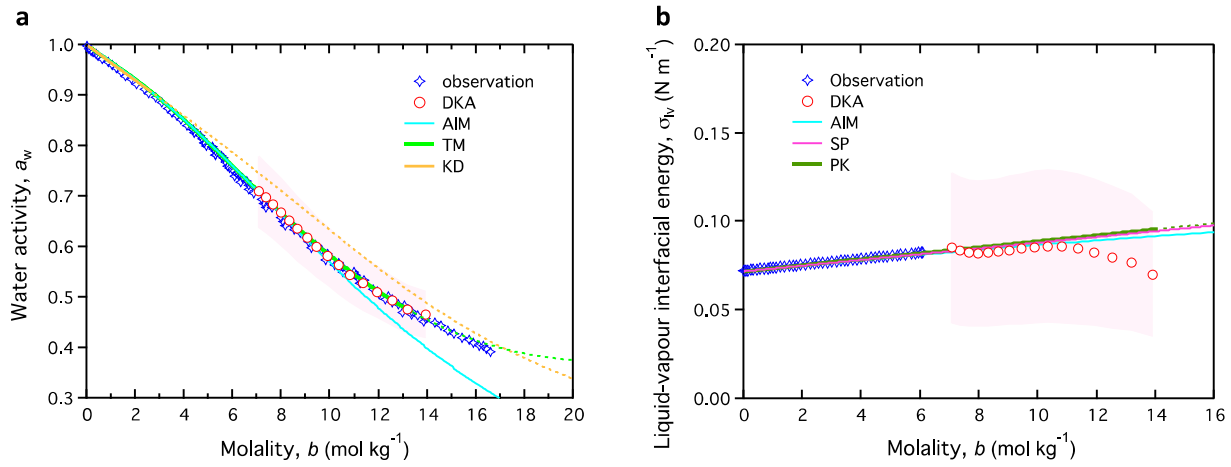

Supplementary Figure 1 | Concentration-dependent water activity and liquid-vapour interfacial energy of aqueous sodium chloride solution. a, b, Water activity (a_w) and liquid-vapour interfacial energy (σ_{lv}) are plotted against solute molality (b). The DKA-derived a_w and σ_{lv} (red open circles) are compared with observations (blue stars)[1-5], Aerosol Inorganic Model[6] (AIM, blue line), and other parameterisations for a_w (TM = Tang-Munkelwitz[7], green line; KD = Kreidenweis[8], orange line) and σ_{lv} (PK = Pruppacher-Klett[5], dark green line; SP = Seinfeld-Pandis[9], purple line) (Supplementary Note 3). Dashed lines indicate extrapolation beyond validated concentration range. Pink shaded areas indicate the uncertainties in the DKA retrieval, estimated by Monte Carlo analyses (Supplementary Note 1).

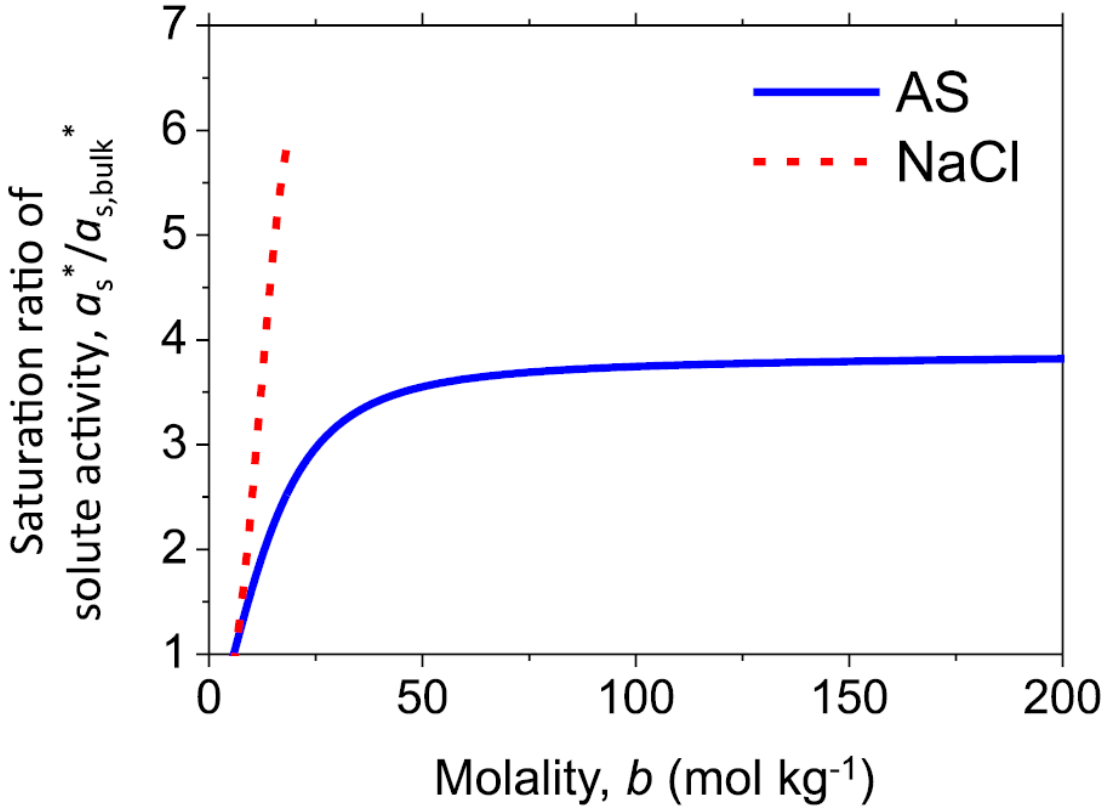

Supplementary Figure 2 | Saturation ratio of solute activity ($a_s^*/a_{s,bulk}^*$) as a function of molality *b* for ammonium sulphate (AS) and sodium chloride (NaCl).

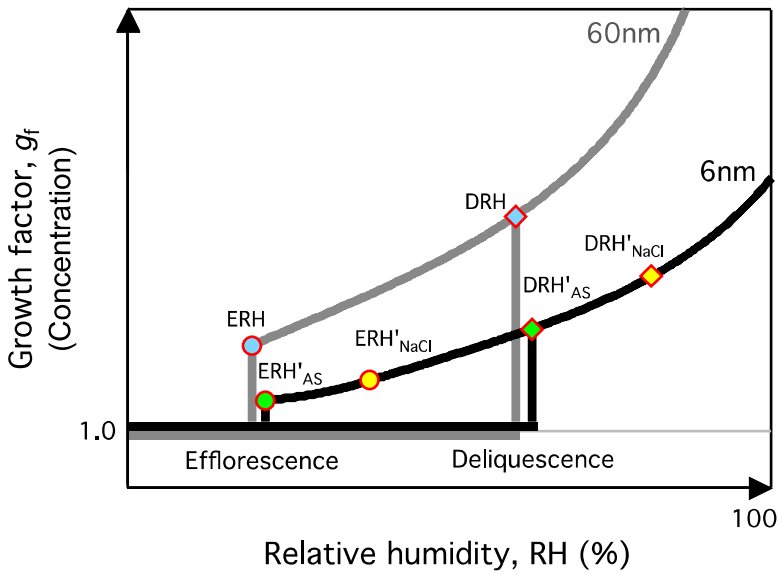

Supplementary Figure 3 | Schematic phase diagram of nanoparticles, exampled for 6-nm and 60-nm. According to Köhler theory, smaller growth is expected for smaller particles upon humidification due to the curvature Kelvin effect. Theoretically, efflorescence of a supersaturated droplet happens when its concentration reaches its characteristic crystallization concentration (molality b_e). The efflorescence relative humidity (ERH) can be determined from b_e along the Köhler curve. If the b_e values (equivalent to the growth factor g_f upon efflorescence, see Supplementary Note 1) are the same for particles of different sizes (size-independent), the ERH will be size-dependent because the Köhler curves do not overlap each other, and vice versa, i.e., if ERH is not size-dependent, b_e and g_f upon efflorescence must be size-dependent. Analogously, similar facts hold for the deliquescence concentration and relative humidity (DRH). Specifically, the phase transition concentrations of ammonium sulphate (AS) increase tremendously when the particle diameter decreases from 60-nm to 6-nm, leading to the almost unchanged DRH and ERH. While for sodium chloride (NaCl), the size dependence of its phase transition concentrations is much weaker than that of AS, resulting in more prominent shift in its ERH and DRH.

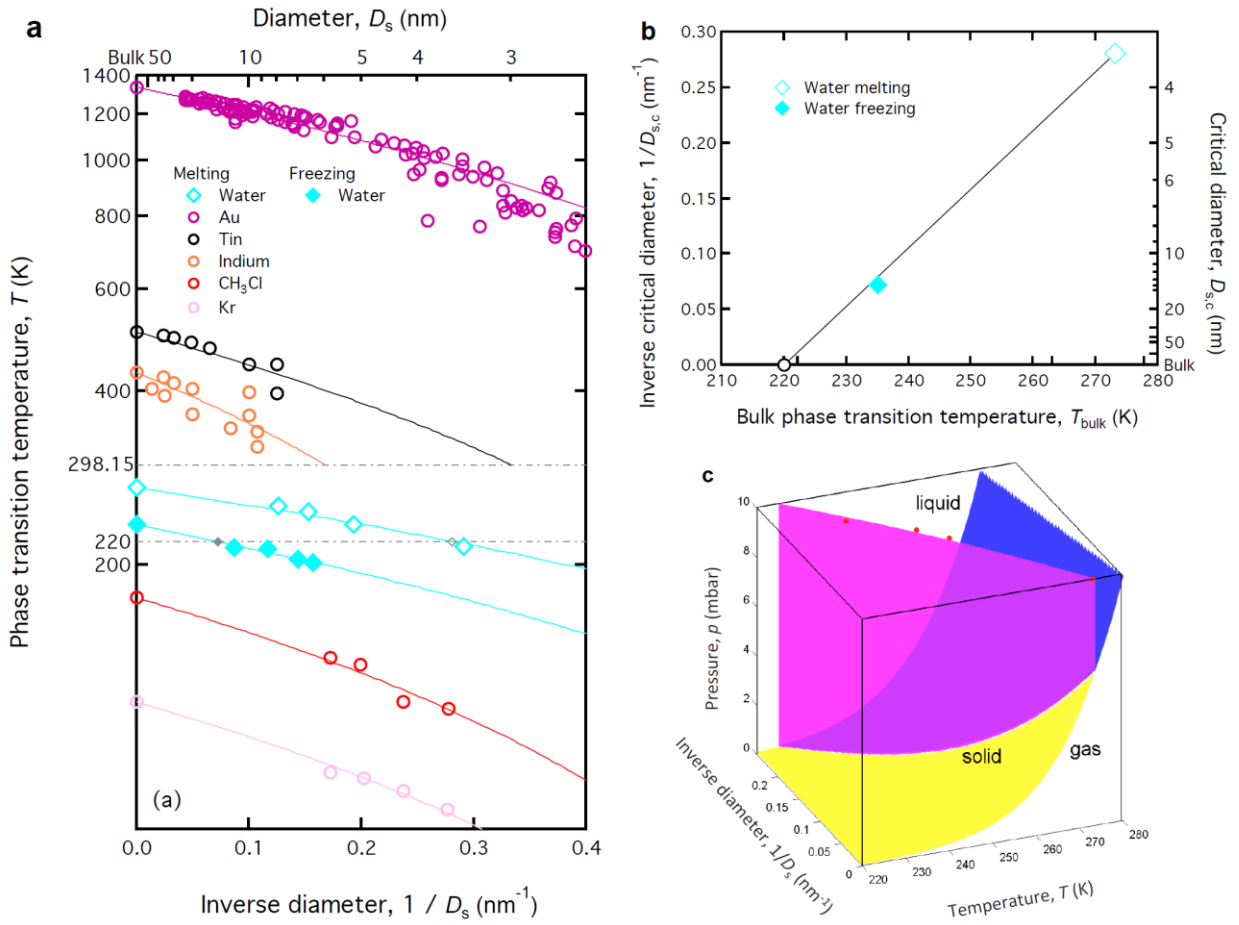

Supplementary Figure 4 | Size effect on various phase transition processes. a, Size-dependent phase transition temperature, such as melting temperature of metals (e.g., Au, Tin and Indium), water, methyl chloride CH_3Cl and Kr, as well as freezing temperature of water[10-16]. **b,** Similar to Fig. 5 but for water at 220 K, corresponding to solid and open grey diamonds on the grey dash line at 220 K in (**a**). The blue solid diamond represents the critical diameter ($D_{s,c}$), which can reduce the freezing temperature of water from 230 K (bulk) to 220 K. The blue open diamond represents the critical diameter, which can reduce the melting temperature of water from 273 K (bulk) to 220 K. They show a rather compact near-linear relationship with the starting point [220 K, D_s^{-1}=0] (black open circle). **c,** 3-D phase diagram for pure water in the coordinates of pressure (p), temperature (T) and inverse diameter (D_s^{-1}). The red solid circles represent the size-dependent melting temperature of water[11]. To facilitate plotting, it is assumed that the size dependence of water melting temperature is independent from pressure change in the most relevant pressure range.

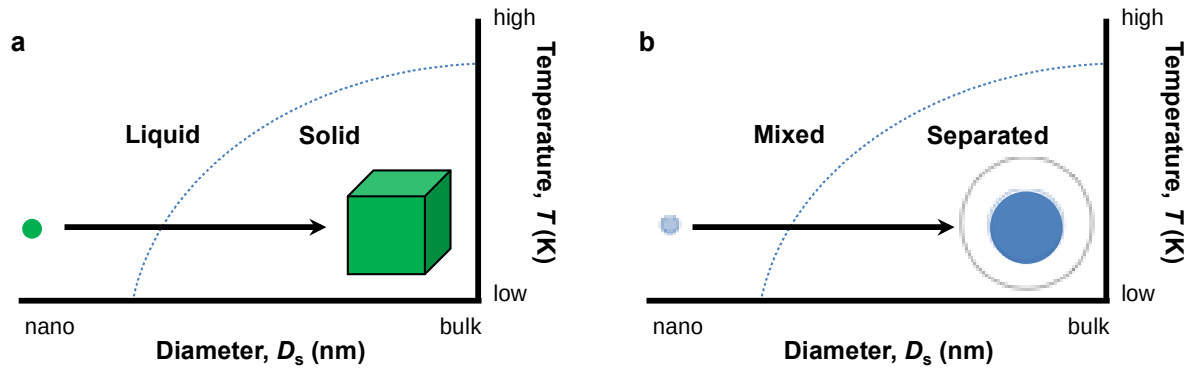

Supplementary Figure 5 | Illustration of size effects on the phase state of pure material (a) and mixed system (b). The dash lines represent the temperature of phase transition/separation as a function of particle size.

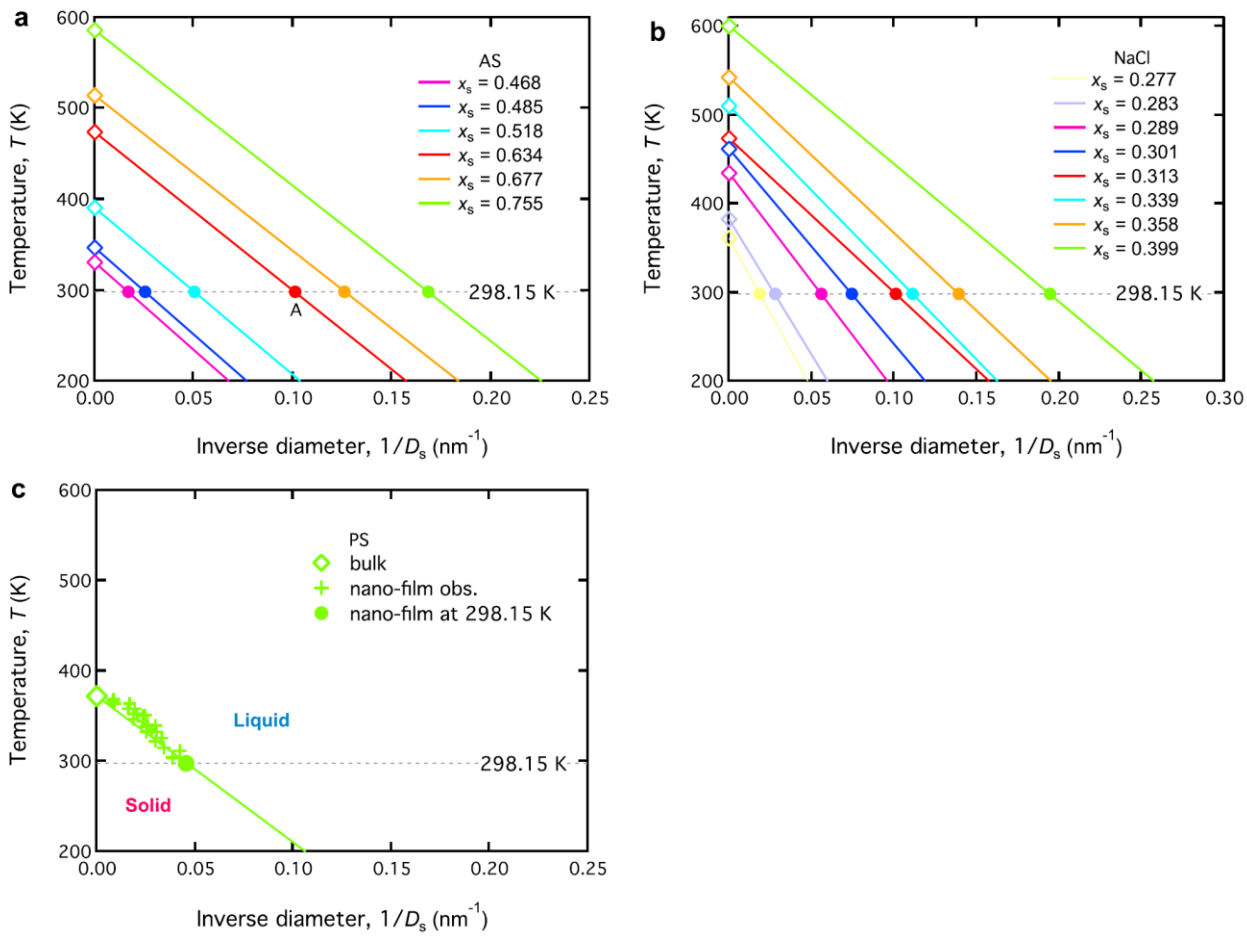

Supplementary Figure 6 | Liquid-solid equilibrium phase diagrams in the coordinate of inverse diameter ($1/D_s$) and phase transition temperature (T) of aqueous ammonium sulphate (AS), aqueous sodium chloride (NaCl) and low chain length polystyrene (PS). a, Slices at different AS mass fractions (x_s) from the 3-D phase diagram of AS-water system (Fig. 4a), similar to the red line in Fig.4e. The x_s values are selected according to the observed solubility of nanoparticles at different sizes. **b,** Similar plot for NaCl-water system. **c,** Size-dependent glass transition temperature of low chain length PS[17].

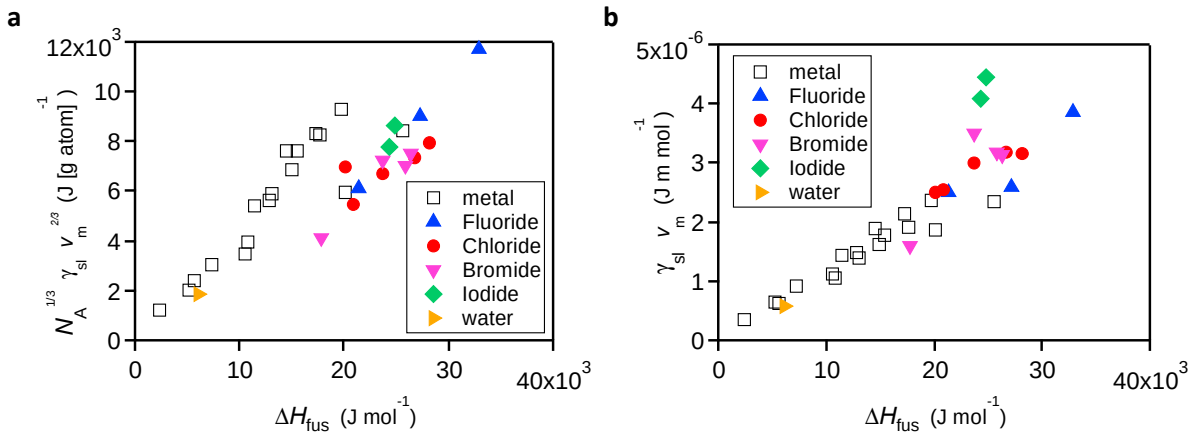

Supplementary Figure 7 | Comparison of enthalpy of fusion (ΔH_{fus}) with interfacial energy of embryo (γ_{sl}). ΔH_{fus} is compared to (**a**) $N_A^{1/3}\gamma_{sl}V_m^{2/3}$ as in Turnbull[18] and (**b**) $\gamma_{sl}V_m$. N_A denotes Avogadro constant, V_m is the molar volume. The metal and water data are taken from Turnbull[18] while the rest are taken from Buckle and Ubbelohde[19,20]. The metals include gold, silver, mercury, lead, etc. The chloride, fluoride, bromide and iodide correspond to LiCl, NaCl, KCl, RbCl, CsCl; LiF, NaF, CsF; LiBr, NaBr, Kbr, CsBr; and KI, CsI, respectively.

Supplementary Tables

Supplementary Table 1 | Fit equations for the DKA-retrieved water activity a_w and liquid-vapour interfacial energy σ_{lv} (N m^{-1}) of ammonium sulphate (AS) at 298K. Here, b is the molality (mol kg^{-1}) and x_s is the AS mass fraction.

Equations	Parameters
$a_w = \frac{A_0 + A_1 x + A_2 x^2}{B_0 + B_1 x + B_2 x^2 + x^3}$ and $x = \frac{b - 13.02}{17.15}$	A_0=46.29; A_1=26.42; A_2=12.51; B_0= 80.77; B_1= 103.6; B_2= 55.09
$\sigma_{lv} = 0.072 + \sum C_i x_s^{\,i}$	C_1= 0.04070; C_2= -0.4627; C_3= 3.799; C_4= -14.46; C_5= 27.80; C_6= -24.63; C_7= 8.016

Supplementary Note 1. Differential Köhler Analysis (DKA)

Shape factor correction for HTDMA measurement data. The results of humidified tandem differential mobility analyzer (HTDMA) were usually reported in the form of the growth factor g_f as a function of water vapour saturation ratio s_w at each dry equivalent spherical mobility diameter D_s. However, g_f and D_s determined by DMA need to be corrected for the particle shape (non-spherical) and porosity. For ammonium sulphate (AS), we adopted the method of Biskos et al.[21], taking a shape factor of 1.02 for the dry AS particle sizes and 1.0 for the wet particle sizes (no correction). For sodium chloride (NaCl) dry particles, we adopted a size-dependent shape factor varying from 1.24 to 1.07 as suggested by DeCarlo et al.[22] and Biskos et al.[23] for 8-nm to 60-nm NaCl nanoparticles. For 6-nm NaCl particles, the same correction method failed to reproduce the observed g_f over the whole hygroscopic growth curve. Biskos et al.[23] suggested that it is due to nanosize effects on thermodynamic properties and/or uncertainties in thermodynamic properties/shape factors. We notice that the deviation still exists for the largest droplet (e.g., with g_f = 1.6 measured at 6-nm and thus D_{sol} = 6×1.6 = 9.6 nm), where the size is beyond the range of significant nanosize effects (on thermodynamic properties). It is likely that the shape factor is the main reason for the deviation.

In the present study, a shape factor of ~1.37 was applied to 6-nm NaCl particles. It was determined by numerically searching for a value that is able to match the observed hygroscopic growth curve with relative humidity (RH) higher than the deliquescence point, an equivalent spherical mobility diameter about 5.14 nm is obtained for the dry particle after this shape factor correction. Considering the measurement uncertainty in RH and g_f, the derived shape factor for 6-nm NaCl particle may vary from 1.28 to 1.45. This is slightly larger than the numerically calculated dynamic shape factor of ideal cubic NaCl particles (~1.24) in the free-molecular flow regime[22,24], which may due to the imperfect nucleation and coagulation[25].

Size dependence of σ_{lv}. It is known that the liquid-vapour interfacial energy (σ_{lv}) depends not only on the solute concentration (mass fraction x_s) but also on the particle size[26],

$$\sigma_{lv} = \varepsilon \, \sigma_{lv,bulk} \tag{1}$$

where $\sigma_{lv,bulk}$ denotes the bulk interfacial energy, and ε denotes the size-dependent curvature adjustment factor. The size-dependence of σ_{lv} will introduce another term $\frac{2v_w}{RT}\frac{d\sigma_{lv}}{dD_{sol}}$ into the Köhler equation. The following deduction will show the origin of this size dependent term.

The change of Gibbs free energy (G) for the creation of a spherical droplet is

$$\Delta G = (\mu_l - \mu_v)\frac{V_w}{v_w} + \sigma_{lv} A_w \tag{2}$$

where μ_l and μ_v represent the chemical potentials of the liquid and its vapor, respectively, σ_{lv} is the liquid-vapour interfacial energy, and A_w is the surface area of the droplet, V_w is the droplet volume, and v_w is the molar volume of the liquid.

The criterion of equilibrium for a system of prescribed temperature and pressure is that ΔG has reached its minimum, so

$$\frac{d\Delta G}{dD} = \frac{(\mu_l - \mu_v)}{v_w}\frac{dV_w}{dD} + \frac{d(\sigma_{lv} A_w)}{dD} = 0 \tag{3}$$

where D is the droplet diameter, then

$$\frac{(\mu_l - \mu_v)}{v_w}\frac{d(\frac{1}{6}\pi D^3)}{dD} + \frac{d(\sigma_{lv}\pi D^2)}{dD} = 0 \tag{4}$$

The difference in the chemical potential is a function of vapor pressure p over the droplet and the equilibrium vapor pressure p^*, $(\mu_l - \mu_v) = -RT\ln(p/p^*)$, so supplementary equation (4) becomes

$$-\frac{RT\ln(\frac{p}{p^*})}{v_w}\frac{1}{2}\pi D^2 + (2\sigma_{lv}\pi D + \pi D^2\frac{d\sigma_{lv}}{dD}) = 0 \tag{5}$$

$$-RT\ln(\frac{p}{p^*})+\frac{4v_w\sigma_{\mathrm{lv}}}{D}+2v_w\frac{d\sigma_{\mathrm{lv}}}{dD}=0 \quad (6)$$

Finally, we have

$$s_{\mathrm{w}}=\exp(\frac{4\sigma_{\mathrm{lv}}v_w}{RTD}+\frac{2v_w}{RT}\frac{d\sigma_{\mathrm{lv}}}{dD}) \quad (7)$$

where $s_{\mathrm{w}} = p/p^*$, and σ_{lv} is a function of the droplet size D. By neglecting the size dependence of σ_{lv}, i.e., $d\sigma_{\mathrm{lv}}/dD=0$, supplementary equation (7) becomes the tradition Kelvin equation

$$s_{\mathrm{w}}=\exp(\frac{4\sigma_{\mathrm{lv}}v_w}{RTD}) \quad (8)$$

In our study, particle sizes are larger than 6 nm. The size dependent term $\frac{2v_w}{RT}\frac{d\sigma_{\mathrm{lv}}}{dD_{\mathrm{sol}}}$ is negligible (<1%) compared to the original term $4\sigma_{\mathrm{lv}}v_{\mathrm{w}}/(RTD_{\mathrm{sol}})$ for the investigated size ranges and is therefore not considered. Substituting supplementary equation (1) into equation (1), the solution in equation (3) becomes

$$a_w=\frac{s_{\mathrm{w1}}^{(\frac{D_{s1}\varepsilon_2}{D_{s1}\varepsilon_2-D_{s2}\varepsilon_1})}}{s_{\mathrm{w2}}^{(\frac{D_{s2}\varepsilon_1}{D_{s1}\varepsilon_2-D_{s2}\varepsilon_1})}} \quad \text{and} \quad \sigma_{lv,bulk}=\frac{D_{s1}D_{s2}\ln\frac{s_{\mathrm{w1}}}{s_{\mathrm{w2}}}}{A(D_{s2}\varepsilon_1-D_{s1}\varepsilon_2)} \quad (9)$$

where $A=4v_{\mathrm{w}}/(RTg_f)$, a_{w} is the water activity, s_{w1} and s_{w2} are water saturation ratios measured at the same g_f but at D_{s1} and D_{s2}, respectively. In this study, ε is calculated according to Bahadur and Russell[26]. However, it is worth noticing that the size dependence of interfacial energy will not play a significant role unless the solution droplets are smaller than 5 to 6 nm[26].

Partial molar volume of water v_{w}. Partial molar volume of water v_{w} can be expressed as a function of solution density[27],

$$v_w=\frac{M_{\mathrm{w}}}{\rho_{\mathrm{sol}}}(1+\frac{d\ln\rho_{\mathrm{sol}}}{d\ln x_{\mathrm{s}}}) \quad (10)$$

where M_w is the molar mass of water, ρ_{sol} is the solution density and x_s is the solute mass fraction.

Conversion of growth factor g_f to solute mass fraction x_s. In this section we show that if the concentrations of droplet solutions are the same, their growth factors g_f would also be identical. The symbols are defined as follows: m_s and m_{sol} are the mass of solute and solution, V_s and V_{sol} are the volume of solute and solution, ρ_s and ρ_{sol} are the density of solute and solution and x_s is the mass fraction of solute, respectively. By definition, we have for spherical particles/droplets of homogeneous composition

$$g_f = \left(\frac{V_{sol}}{V_s}\right)^{1/3} = \left(\frac{m_{sol}}{\rho_{sol} V_s}\right)^{1/3} = \left(\frac{m_s}{x_s \rho_{sol} V_s}\right)^{1/3} = \left(\frac{V_s \rho_s}{x_s \rho_{sol} V_s}\right)^{1/3} = \left(\frac{\rho_s}{x_s \rho_{sol}}\right)^{1/3} \quad (11)$$

Here, ρ_s is a constant and ρ_{sol} is a function of solution concentration x_s. Therefore, for a specific solute/solutes and with the assumption of a size-independent solution density of spherical particles, the same x_s in general means the same g_f and vice versa. Note that, nano-size effects on the density itself can result in a change in the density when the size gets really small. Such effects are, however, trivial (<1%) above a threshold diameter ~1 nm to 5 nm[23,28], and are therefore negligible for 6 nm to 60 nm particles investigated in the present study.

The smallest growth factor of 6-nm ammonium sulphate particle observed by the HTDMA experiments during dehydration prior to crystallization is about 1.04 (upon efflorescence of 6-nm ammonium sulphate particle)[21], which corresponds to a molality b of ~380 mol kg^{-1}. However, the retrieval using DKA is limited by the highest overlapped concentrations, corresponding to b ~160 mol kg^{-1} (x_s ~0.96).

Uncertainty analyses with Monte-Carlo simulation. To properly estimate the uncertainty of the proposed DKA method, we performed a Monte Carlo simulation by randomly varying all or a section of input parameters/data for the retrievals. Deviations for these input parameters/data were considered to be normally distributed around the original value with one relative standard deviation (*std*). A range of ±3*std* around the original value contains 99% of the values possible for the input parameter/data point according to the respective uncertainty due to assumptions in

the parameterization or arisen from the experiments, which represent a conservative estimate of the maximum uncertainties and ensure that the overall uncertainty estimation is not based on excessively large outliers. The uncertainties of the different input parameters and data are summarised here as: ±2% for relative humidity (RH), ±1% for dry diameter sizing (D_s) of AS, ±5% for D_s of NaCl due to shape factor uncertainties, ±1% for wet diameter sizing (D_{sol}), ±2.5% for growth factor (g_f) [21, 23].

40,000 runs of retrieval calculations were tested to be sufficient for convergence of the mean value and of the standard deviation. The discrepancy between the expected mean value of those 40,000 runs and the calculated value without any uncertainty variation of the inputs is less than 0.5%. Consequently, the retrieval calculations of σ_{lv} and a_w were made by randomly choosing 20,000 different sets of input parameters and data (such as diameter, growth factor, and relative humidity). Three times relative standard deviation (±3*std*) of the results from those 40,000 runs are considered as uncertainties (at 99% confidence level) for the output of the DKA method (i.e., a_w and σ_{lv}).

Supplementary Note 2. Determination of a_s, σ_{ls} and γ_{ls}

The solute activity a_s on a mole fraction basis is calculated by the Gibbs-Duhem equation[9,29,30] at constant temperature and pressure, where n_s and n_w represent the mole fraction of solute and water, respectively

$$n_s d\ln a_s + n_w d\ln a_w = 0 \tag{12}$$

Integrating supplementary equation (12) from $x_{s,bulk}^*$ to x_s

$$\ln \frac{a_s}{a_{s,bulk}^*} = -\int_{x_{s,bulk}^*}^{x_s} \frac{n_w}{n_s} d\ln a_w \tag{13}$$

where $x_{s,bulk}^*$ is the mass fraction of solute in a saturated bulk solution, and $a_{s,bulk}^*$ is the solute activity at $x_{s,bulk}^*$. Based on the retrieved a_w, we evaluated the integral in supplementary equation (13) numerically and extended it to the same concentration range as a_w.

The interfacial energy at the solid-liquid interface σ_{sl} is determined by the Ostwald-Freundlich equation [31,32] as

$$\sigma_{sl} = \frac{m_i \rho_s RTD_s}{4M_s} \ln \frac{a_s^*}{a_{s,bulk}^*} \tag{14}$$

where a_s^* is the solute activity in a solution saturated with respect to salt particles of diameter D_s, M_s is molar weight of solute, ρ_s is the density of solute and m_i is the stoichiometric number of dissociated ions. In this study, a_s^* is determined from deliquescence of salt nanoparticles by the Köhler equation and the Gibbs-Duhem equation. According to Chen[33], deliquescence of salt particle of D_s happens when the ambient s_w equals the equilibrium s_w over a droplet of the size D_s and saturated with respect to crystalline salt particles of size D_s. In practice, this equilibrium s_w is the onset deliquescence s_w (equivalent to deliquescence relative humidity, DRH) and can be determined by HTDMA measurements. Since s_w (=DRH) and D_{sol} (=D_s) are known, the equilibrium concentration b^* can be determined by equation (1) and b^* represents the saturation molality with respect to D_s. Then a_s^* and σ_{sl} can be determined. The size dependence of σ_{sl}

shows negligible impact on the simulation, i.e., <0.5% differences in the predicted μ_{del} and <0.2% differences in the DRH. It is hence neglected in our simulation.

The interfacial energy of solute embryo γ_{sl} is determined by the classical nucleation theory as Cohen et al.[29] and Gao et al.[34,35].

$$\gamma_{sl} = \left[\frac{4(\sum_j k_j)\alpha^2}{27\Delta G_v^{\ 2} k_b T}\ln(V_{sol} K t_i)\right]^{-1/3} \quad (15)$$

where k_j and α are geometrical constants dependent on the morphology of the particular crystal, ΔG_v is the excess free energy of solute per unit volume in the crystalline phase over that in solution, k_b is the Boltzmann constant, V_{sol} is the volume of the droplet, K is the pre-exponential factor, and t_i is the induction time interval (taken as 2 second for the HTDMA measurements[21]). All parameters except a_w and a_s in supplementary equation (15) were taken the same as in Cohen et al.[29]. It is still on debate if a closure should be expected between σ_{sl} and γ_{sl}[25]. We found that $\sigma_{sl} > \gamma_{sl}$ for the investigated AS and NaCl salts particles which seems to hold for other compounds (e.g. $BaSO_4$) as well[36]. The fact that $\sigma_{sl} > \gamma_{sl}$ appears to be in line with the general size dependence of interfacial energies[26]: decreasing interfacial energy is expected for embryos of sizes ~1 nm[29] while no significant difference is expected for particles larger than 6 nm.

Supplementary Note 3. Thermodynamic models and parameterizations

Overview of model selection. In the following, we listed the reasons why the particular models were chosen for model prediction and comparison in our study:

(1) To represent the current study

We use newly determined a_w and σ_{lv} by the DKA method for AS. These data agree very well with literature observation data and also largely extend the concentration beyond the observation and existing parameterization methods as shown in Fig. 2.

For NaCl, we use a_w from the modified TM model (more details as given below) and σ_{lv} from the PK model[5]. This is because the DKA method suffers from uncertainties in the shape factor correction for NaCl particles, and the modified TM and PK agrees well with the DKA derived a_w and σ_{lv} for NaCl, as shown in Supplementary Fig. 1. The good agreement between modeled and observed deliquescence/efflorescence (Fig. 1) also confirms the reliability of modified TM and PK in the investigated concentration range.

The modified TM adopts the same expression as the original TM model[7] for the validated concentration range (x_s<0.45) and used an expression

$$a_w = \frac{0.1703 \cdot x_s^2 - 0.6018 \cdot x_s + 0.4315}{x_s^2 - 0.4594 \cdot x_s + 0.4343} \tag{16}$$

for higher concentration range (x_s>0.45), which is constrained by available measurement data and the point [x_s=1, a_w=0]. The main reason for using supplementary equation (16) instead of the original TM is because the later model produces unrealistic results (a_w>1) at x_s>0.45.

(2) To represent Biskos et al.

We choose the original model used by Biskos et al.[21,23], i.e., a combination of TM and PK to represent their study. The molar volume of pure water was used instead of the partial molar volume as in Biskos et al.[21,23].

(3) AIM

The AIM growth curves in Fig. 1 are based on a_w and σ_{lv} from AIM (Aerosol Inorganics Model). There are two reasons for choosing AIM. First, AIM is one of the most commonly used and powerful models for studying the thermodynamic of inorganic aerosols. Second, AIM has the capacity to model highly supersaturated solution[37], providing a good reference under conditions where no measurement data are available. Such comparison could help to illustrate the performance of our method and its potential in improving the AIM model for highly supersaturated solution.

(4) Further comparison of different parameterization methods

Moreover, the TM and PK models are based on the best fit to the literature measurement data of a_w and σ_{lv} (Fig. 2 and Supplementary Fig. 1). As shown in Fig. 2a and Supplementary Fig. 1a, the agreement with measured a_w is better for the TM model than for the KD model[8] and AIM. The KD model is only used as a complete and proper reference to previous work.

The SP model[9] and the PK model were proposed to describe the concentration dependence of σ_{lv}. For NaCl, their difference is not significant within the concentration range of our simulation (Supplementary Fig. 1b). In Fig. 1, we showed only one simulation for clarity.

Aerosol Inorganics model (AIM). Aerosol Inorganics Model-III can be used to model the water activity a_w, liquid-vapour interfacial energy σ_{lv}, and density ρ_{sol} of aqueous solutions at certain temperature (e.g., 298.15K) (http://www.aim.env.uea.ac.uk/aim/model3/model3a.php)[6]. For ammonium sulphate and sodium chloride, the solute molality b, as well as ρ_{sol} and σ_{lv}, can be calculated on-line by prescribing the bulk solution water activity (a_w as a series of RH ranging from 0.1 to 0.9999).

***a_w* parameterization model I (KD).** Kreidenweis et al.[8] proposed an empirical parameterization, which relates the water activity of AS and NaCl solution with g_f determined in hygroscopic growth measurements:

$$g_f = \frac{D_{sol}}{D_s} = \left(1 + \left(\sum_q k_q a_w^{q-1}\right)\frac{a_w}{1-a_w}\right)^{\frac{1}{3}} \quad (17)$$

The coefficients k_q for AS are k_1 = 2.42848, k_2 = -3.85261, and k_3 = 1.88159. The respective coefficients for NaCl are k_1 = 5.78874, k_2 = -8.38172, and k_3 = 3.9265. The method was demonstrated by HTDMA measured hygroscopic data for dry AS and NaCl particles with spherical equivalent mobility diameter of 100 nm. By comparing with observational data and AIM modelling results, this parameterized relationship was validated for the AS and NaCl solution droplets at $x_s < 0.3$ and $x_s < 0.13$, respectively[8]. Thus, with each single measurement of g_f of dry AS and NaCl particle, one could retrieve the corresponding a_w by iteratively solving supplementary equation (17).

a_w parameterization model II (TM). Tang and Munkelwitz[7,38] presented parameterizations of water activity a_w in aqueous solution droplet of AS and NaCl derived from single particle experiments by the EDB (Electrodynamic Balance method). The parameterization of a_w is expressed as polynomial fit functions of solute mass fraction (x_s):

$$a_w = 1 + \sum_q A_q (100 \cdot x_s)^q \quad (18)$$

The polynomial coefficients A_q for AS at 298 K are $A_1 = -2.175\times10^{-3}$, $A_2 = 3.113\times10^{-5}$, $A_3 = -2.336\times10^{-6}$, and $A_4 = 1.412\times10^{-8}$. The respective coefficients for NaCl are $A_1 = -6.366\times10^{-3}$, $A_2 = 8.624\times10^{-5}$, $A_3 = -1.158\times10^{-5}$, and $A_4 = 1.518\times10^{-7}$. According to the EDB experiments[7,38], the validated range of this parameterization method is $x_s < 0.78$ for AS and $x_s < 0.45$ for NaCl. It is used by Biskos et al.[21,23] to predict their measured hygroscopic growth curve (against RH) of nano-sized AS and NaCl particles.

σ_{lv} parameterization model I (SP). Seinfeld and Pandis[9] proposed the following parameterization for the liquid-vapour interfacial energy of aqueous salt solution droplets:

$$\sigma_{\mathrm{lv}} = \sigma_w + k_s c_{\mathrm{s}} \tag{19}$$

in which $k_{\mathrm{s}} = 2.17\times10^{-3}$ N m^{-1} L mol^{-1} for AS and $k_{\mathrm{s}} = 1.62\times10^{-3}$ N m^{-1} L mol^{-1} for NaCl. c_{s} is the molarity of the solution, which is defined as the amount of substance divided by the volume of the solution in units of mol L^{-1}. σ_{w} is the surface density of pure water. In the present study, σ_{w} is treated as temperature-dependent and is described by[9]:

$$\sigma_{\mathrm{w}} = 0.0761 - 1.55\times10^{-4}(T - 273.15) \tag{20}$$

σ_{lv} parameterization model II (PK). Pruppacher and Klett[5] proposed another parameterization for σ_{lv} of aqueous AS and NaCl solutions as

$$\sigma_{\mathrm{lv}} = 0.072 + \frac{2.34\times10^{-2}\cdot x_s}{1 - x_s} \qquad \text{for AS} \tag{21}$$

$$\sigma_{\mathrm{lv}} = 0.072 + \frac{2.9\times10^{-2}\cdot x_s}{1 - x_s} \qquad \text{for NaCl} \tag{22}$$

of which the validated range is $x_{\mathrm{s}} < 0.78$ for AS and $x_{\mathrm{s}} < 0.45$ for NaCl[24]. It is used by Biskos et al.[21,23] to predict their measured hygroscopic growth curve (against RH) of nano-sized AS and NaCl particles.

Solution density ρ_{sol}. In the present study, the concentration-dependent solution densities of AS and NaCl are parameterized based on the EDB measurements[7,38] as polynomial fit functions of solute mass fraction x_{s}:

$$\rho_{sol} = \rho_w + \sum_q d_q (100\cdot x_s)^q \tag{23}$$

The polynomial coefficients d_{q} for AS at 298 K are $d_1 = 5.92$, $d_2 = -5.036\times10^{-3}$, and $d_3 = 1.024\times10^{-5}$. The respective coefficients for NaCl are $d_1 = 7.41$, $d_2 = -3.741\times10^{-2}$, $d_3 = 2.252\times10^{-3}$,

and d_4 = -2.06×10^{-5}. Here ρ_w is the density of pure water in kg m^{-3}. In the present study, a temperature-dependent ρ_w is used[5]:

$$\rho_w = \frac{\sum_q A_q \cdot (T - 273.15)^{q-1}}{1 + B \cdot (T - 273.15)} \quad (24)$$

where T is the temperature in K. The coefficients A_q are A_1 = 999.8396, A_2 = 18.224944, A_3 = -7.92221×10^{-3}, A_4 = -55.44846×10^{-6}, A_5 = 149.7562×10^{-9}, and A_6 = -393.2952×10^{-12}. The coefficient B is 18.159725×10^{-3}.

Since we are dealing with highly supersaturated AS solution, we adopted a parameterization suggested by Clegg and Wexler[39] in which the extended solution density was constrained by the density of molten salt. The density of molten AS is estimated to be ~1.61×10^3 kg m^{-3} at 298.15K. It shows general good agreement with non-constrained density parameterization[38,39] when x_s is below ~0.45, but when x_s approaches 1.0, the deviations increases to up to 3-4%[39]. We also found that the smallest growth factor of 6-nm AS particles observed during dehydration prior to crystallization (g_f ~1.041, corresponding to a AS:H_2O molar ratio of 7:1)[21] cannot be explained by the non-constrained AS solution density. The minimum ρ_{sol} required to explain such small g_f is ~1.57×10^3 kg m^{-3}, falling into the range of the ρ_{sol} constraint by the molten salt properties.

Disjoining pressure. Among earlier efforts to explain the deliquescence/efflorescence, Djikaev et al.[40] and Shchekin et al.[41] introduced a "disjoining pressure" in their models. The effect of "disjoining pressure" makes the existence of partially dissolved solute possible, which will result in a continuous deliquescence as RH increases. To explain the continuous deliquescence is one of the major goals of introducing the disjoining pressure in Djikaev et al.[40]. In other words, a prompt deliquescence would suggest that the solute is fully dissolved and the effect of disjoining pressure is negligible[40]. This is exactly the case for the HTDMA data that we were using. Therefore, the disjoining pressure was not considered in our model simulation. The negligibility of the disjoining pressure was further confirmed by the good agreement between the observation and our model prediction.

Supplementary Note 4. Melting temperature of atmospheric biogenic secondary organic aerosols

Cappa and Wilson[42] indicate that the secondary organic aerosol (SOA) particles with median volume weighted diameter of ~100 nm formed through α-pinene ozonolysis might be in a solid amorphous state rather than liquid. On the other hand, bouncing experiments clearly show that particle bounce decreases with decreasing particle size in sub 30 nm size range, suggesting a different phase state of larger (> 30 nm, solid-like) and smaller (17-30 nm, liquid-like) particles[43,44]. In order to explore the size effect on the biogenic SOA particles (such as pine-derived SOA) and to estimate the relevant critical diameter range that is able to depress its melting temperature down to the ambient conditions (~298 K) according to the T_{bulk}-$D_{s,c}$ relationship (Fig. 5), we need to know the general melting temperature range of such biogenic SOA particles. The relatively low-volatility oxidation products of pinenes include multifunctionalized acids, such as pionic acid, pinic acid, 1,2,3-propane-tricarboxylic acid, 1,2,4-butane-tricarboxylic acid, 3-methyl-1,2,3-butane-tricarboxylic acid, etc. Koop et al.[45] summarized the melting temperature of some of these oxidation products in the range of ~378-439 K. They also estimated that the glass transition temperature (T_g) of pinene-derived SOA in the range of ~240-300 K, and the ratio between glass transition and melting temperature is about 0.7. So, the melting temperature of pinene-derived SOA can be calculated to be about 340-430 K, accordingly. Combining these two ranges, we consider the melting temperature range of pinene-derived SOA to be in the range of 340 K to 440 K, as a conservative estimation.

Supplementary Discussion. Heuristic viewpoint concerning the phase transition

In this section, we will discuss the size dependence of phase transition concerning the following aspects: (1) the relationship between different compounds, (2) the relationship between different phase transition processes (melting, glass transition, etc.), and (3) an outlook for future work in these directions.

(1) Relationship between different compounds

The similarity in the T_{bulk}-$D_{s,c}$ relations suggests the following supplementary equation (25), a close relationship between σ_{sl} (the interfacial energy at the solid-liquid interface) and ΔH (enthalpy of phase transition)

$$\frac{\sigma_{sl} V_m}{\Delta H} \approx \text{constant} \tag{25}$$

where V_m is the molar volume of solid. The deduction of supplementary equation (25) is as follows. According to the Gibbs-Thomson equation, the depression of phase transition (melting) temperature ΔT of particles of diameter D is

$$\Delta T = T_{bulk} - T(D) = T_{bulk} \frac{4\sigma_{sl} V_m}{\Delta H D} \tag{26}$$

$$1 - \frac{T(D)}{T_{bulk}} = \frac{4\sigma_{sl} V_m}{\Delta H D} \tag{27}$$

$$f(T_{bulk}) = (\frac{4\sigma_{sl} V_m}{\Delta H}) D^{-1} \tag{28}$$

As shown in Fig. 5, data pairs (T_{bulk}, $D_{s,c}^{-1}$) of different compounds/systems (salts, organics and SOA) converge onto a compact correlation. It means that

$$D_i \approx D_j \Rightarrow T_{bulk,i} \approx T_{bulk,j} \tag{29}$$

According to supplementary equation (28), the validation of supplementary equation (29) would require $\frac{\sigma_{sl}V_m}{\Delta H} \approx$ constant, suggesting a close relationship between the interfacial energy and the enthalpy of phase transition. This relationship, supplementary equation (25), reminds us the Turnbull empirical equation[18]

$$\frac{\sigma_{sl}V_m^{2/3}}{\Delta H} \approx \text{constant} \quad (30)$$

which differs slightly from our equation by a cube root of V_m. For comparison, we reanalyse the data of Turnbull[18] along with corresponding data for molten salts (Supplementary Fig. 7a). We find these data also fit well to our equation (Supplementary Fig. 7b). Note that Supplementary Fig. 7 contains a variety of metals (17 metals such as mercury, gold, silver, lead, etc) and molten salts, and our results contain organics and different water-salt mixed systems. These facts give us confidence that we might be able to generalize supplementary equation (25) for a large number of compounds in both melting and dissolution processes.

(2) Relationship between different phase transition processes

Beside dissolution and melting processes, size dependence has been found for other phase transition processes, such as glass transition, nucleation and spinodal decomposition[46] (Supplementary Fig. 4 and references therein). There are few studies providing size dependent data from different phase transition processes for the same compound. The freezing and melting temperatures of water in Supplementary Fig. 4 are the only data we found in literature. The measured T_m (melting temperature) and simulated T_f (freezing temperature) show very similar size dependence. The reason for the similarity is still not clear, but it has been found that the characteristic temperatures for different phase transition processes often show simple relations. For example, $T_g \approx 0.7 * T_m$ [45] and $T_f \approx 0.82 * T_m$ [18], despite of different theories involved (thermodynamics equilibrium for melting and nucleation theory for freezing). If such relations hold at each size range, i.e.,

$$T_g(D) = 0.7 * T_m(D) \quad \text{and} \quad T_f(D) = 0.82 * T_m(D) \quad (31)$$

substituting it into supplementary equation (27) would give

$$1-\frac{T_g(D)}{T_{\mathrm{bulk},g}}=\frac{4\sigma_{\mathrm{sl}}V_m}{\Delta HD} \qquad \text{and} \qquad 1-\frac{T_f(D)}{T_{\mathrm{bulk},f}}=\frac{4\sigma_{\mathrm{sl}}V_m}{\Delta HD} \tag{32}$$

which shows similar size dependence as for the melting temperature. Supplementary equation (32) would support the similarity of T_{bulk}-$D_{\mathrm{s,c}}$ relationship between different phase transition processes.

(3) Outlook and future work

Size dependence could provide further insight into the underlying mechanisms of phase transition and should be pursued more extensively. In the past, size dependent phase transitions have been studied for different compounds. Here, we would expect a deeper insight from size dependence measurements of different phase transition processes for the same substance. Such measurements would provide another dimension to validate, improve and possibly reconcile the various existing theories for different phase transition phenomena (such as melting, nucleation, spinodal decomposition, glass transition, dissolution, etc.).

It is known that the interaction with a substrate can significantly change the size dependence of phase transitions for investigated samples. To properly account for or to avoid interaction with a substrate is essential for the comparison and synthetic studies aforementioned. The substrate-free methods based on the tandem DMA as demonstrated in this study provides a new experimental tool in this direction. Molecular dynamics simulations will be a key modelling tool in reconciling the mechanisms leading to size dependence of different phase transition processes.

Supplementary References

1 Archer, D. G. Thermodynamic Properties of the NaCl+H_2O System. II. Thermodynamic Properties of NaCl(aq), NaCl-2H_2O(cr), and Phase Equilibria. *J. Phys. Chem. Ref. Data* **21**, 793-829 (1992).

2 Chan, C. K., Liang, Z., Zheng, J., Clegg, S. L. & Brimblecombe, P. Thermodynamic Properties of Aqueous Aerosols to High Supersaturation: I - Measurements of Water Activity of the System Na^+−Cl^-−NO_3^-−SO_4^{2-}−H_2O at ~ 298.15 K. *Aerosol Sci. Tech.* **27**, 324-344 (1997).

3 Clegg, S. L., Brimblecombe, P., Liang, Z. & Chan, C. K. Thermodynamic Properties of Aqueous Aerosols to High Supersaturation: II—A Model of the System Na^+−Cl^-−NO^{-3}−SO_4^{2-}−H_2O at 298.15 K. *Aerosol Sci. Tech.* **27**, 345-366 (1997).

4 Tang, I. N., Munkelwitz, H. R. & Wang, N. Water activity measurements with single suspended droplets: The NaCl-H2O and KCl-H2O systems. *J. Colloid Interf. Sci.* **114**, 409-415 (1986).

5 Pruppacher, H. R. & Klett, J. D. *Microphysics of clouds and precipitation*. (Kluwer Academic Publishers, 1997).

6 Clegg, S. L., Brimblecombe, P. & Wexler, A. S. Thermodynamic Model of the System H^+−NH_4^+−Na^+−SO_4^{2-}−NO_3^-−Cl^-−H_2O at 298.15 K. *J. Phys. Chem. A* **102**, 2155-2171 (1998).

7 Tang, I. N. Chemical and size effects of hygroscopic aerosols on light scattering coefficients. *J. Geophys. Res-Atmos.* **101**, 19245-19250 (1996).

8 Kreidenweis, S. M. *et al.* Water activity and activation diameters from hygroscopicity data - Part I: Theory and application to inorganic salts. *Atmos. Chem. Phys.* **5**, 1357-1370 (2005).

9 Seinfeld, J. H. & Pandis, S. N. *Atmospheric Chemistry and Physics, from Air Pollution to Climate Change*. (John Wiley, 2006).

10 Couchman, P. R. & Jesser, W. A. Thermodynamic theory of size dependence of melting temperature in metals. *Nature* **269**, 481-483 (1977).

11 Pan, D., Liu, L.-M., Slater, B., Michaelides, A. & Wang, E. Melting the Ice: On the Relation between Melting Temperature and Size for Nanoscale Ice Crystals. *ACS Nano* **5**, 4562-4569 (2011).

12 Buffat, P. & Borel, J. P. Size effect on the melting temperature of gold particles. *Phys. Rev. A* **13**, 2287-2298 (1976).

13 Morishige, K. & Kawano, K. Freezing and Melting of Methyl Chloride in a Single Cylindrical Pore: Anomalous Pore-Size Dependence of Phase-Transition Temperature. *J. Phys. Chem. B* **103**, 7906-7910 (1999).

14 Morishige, K. & Kawano, K. Freezing and Melting of Nitrogen, Carbon Monoxide, and Krypton in a Single Cylindrical Pore. *J. Phys. Chem. B* **104**, 2894-2900 (2000).

15 Manka, A. *et al.* Freezing water in no-man's land. *Phys. Chem. Chem. Phys.* **14**, 4505-4516 (2012).

16 Li, T., Donadio, D. & Galli, G. Ice nucleation at the nanoscale probes no man's land of water. *Nat Commun* **4**, 1887 (2013).

17 Forrest, J. A. & Mattsson, J. Reductions of the glass transition temperature in thin polymer films: Probing the length scale of cooperative dynamics. *Phys. Rev. E* **61**, R53-R56 (2000).

18 Turnbull, D. Formation of Crystal Nuclei in Liquid Metals. *J. Appl. Phys.* **21**, 1022-1028 (1950).

19 Buckle, E. R. & Ubbelohde, A. R. Studies on the Freezing of Pure Liquids. I. Critical Supercooling in Molten Alkali Halides. *P. Roy. Soc. Lond. A Mat.* **259**, 325-340 (1960).

20 Buckle, E. R. & Ubbelohde, A. R. Studies on the Freezing of Pure Liquids. III. Homogeneous Nucleation in Molten Alkali Halides. *P. Roy. Soc. Lond. A Mat.* **261**, 197-206 (1961).

21 Biskos, G., Paulsen, D., Russell, L. M., Buseck, P. R. & Martin, S. T. Prompt deliquescence and efflorescence of aerosol nanoparticles. *Atmos. Chem. Phys.* **6**, 4633-4642 (2006).

22 DeCarlo, P. F., Slowik, J. G., Worsnop, D. R., Davidovits, P. & Jimenez, J. L. Particle Morphology and Density Characterization by Combined Mobility and Aerodynamic Diameter Measurements. Part 1: Theory. *Aerosol Sci. Tech.* **38**, 1185-1205 (2004).
23 Biskos, G., Russell, L. M., Buseck, P. R. & Martin, S. T. Nanosize effect on the hygroscopic growth factor of aerosol particles. *Geophys. Res. Lett.* **33**, L07801 (2006).
24 Dahneke, B. E. Slip correction factors for nonspherical bodies—III the form of the general law. *J. Aerosol Sci.* **4**, 163-170 (1973).
25 Erdemir, D., Lee, A. Y. & Myerson, A. S. Nucleation of Crystals from Solution: Classical and Two-Step Models. *Accounts Chem. Res.* **42**, 621-629 (2009).
26 Bahadur, R. & Russell, L. M. Effect of Surface Tension from MD Simulations on Size-Dependent Deliquescence of NaCl Nanoparticles. *Aerosol Sci. Tech.* **42**, 369-376 (2008).
27 Brechtel, F. J. & Kreidenweis, S. M. Predicting Particle Critical Supersaturation from Hygroscopic Growth Measurements in the Humidified TDMA. Part I: Theory and Sensitivity Studies. *J. Atmos. Sci.* **57**, 1854-1871 (2000).
28 Gilbert, B., Huang, F., Zhang, H., Waychunas, G. A. & Banfield, J. F. Nanoparticles: Strained and Stiff. *Science* **305**, 651-654 (2004).
29 Cohen, M. D., Flagan, R. C. & Seinfeld, J. H. Studies of concentrated electrolyte solutions using the electrodynamic balance. 3. Solute nucleation. *J. Phys. Chem.* **91**, 4583-4590 (1987).
30 Richardson, C. B. & Snyder, T. D. A Study of Heterogeneous Nucleation in Aqueous Solutions. *Langmuir* **10**, 2462-2465 (1994).
31 Ostwald, W. Über die vermeintliche Isomerie des roten und gelben Quecksilbersoxyds und die Oberflächenspannung fester Körper. *Z. Phys. Chem.* **34**, 495-503 (1900).
32 Freundlich, H. *Kapillarchemie. Eine Darstellung der Chemie der Kolloide und verwandter Gebiete*. (Akademische Verlagsgesellschaft, 1909).
33 Chen, J.-P. Theory of Deliquescence and Modified Köhler Curves. *J. Atmos. Sci.* **51**, 3505-3516 (1994).
34 Gao, Y., Chen, S. B. & Yu, L. E. Efflorescence Relative Humidity for Ammonium Sulfate Particles. *J. Phys. Chem. A* **110**, 7602-7608 (2006).
35 Gao, Y., Chen, S. B. & Yu, L. E. Efflorescence relative humidity of airborne sodium chloride particles: A theoretical investigation. *Atmos. Environ.* **41**, 2019-2023 (2007).
36 Wu, W. & Nancollas, G. H. Determination of interfacial tension from crystallization and dissolution data: a comparison with other methods. *Adv. Colloid Interfac.* **79**, 229-279 (1999).
37 Dutcher, C. S., Ge, X., Wexler, A. S. & Clegg, S. L. An Isotherm-Based Thermodynamic Model of Multicomponent Aqueous Solutions, Applicable Over the Entire Concentration Range. *J. Phys. Chem. A* **117**, 3198-3213 (2013).
38 Tang, I. N. & Munkelwitz, H. R. Water activities, densities, and refractive indices of aqueous sulfates and sodium nitrate droplets of atmospheric importance. *J. Geophys. Res-Atmos.* **99**, 18801-18808 (1994).
39 Clegg, S. L. & Wexler, A. S. Densities and Apparent Molar Volumes of Atmospherically Important Electrolyte Solutions. 1. The Solutes H_2SO_4, HNO_3, HCl, Na_2SO_4, $NaNO_3$, NaCl, $(NH_4)_2SO_4$, NH_4NO_3, and NH_4Cl from 0 to 50 °C, Including Extrapolations to Very Low Temperature and to the Pure Liquid State, and $NaHSO_4$, NaOH, and NH_3 at 25 °C. *J. Phys. Chem. A* **115**, 3393-3460 (2011).
40 Djikaev, Y. S. *et al.* Theory of size dependent deliquescence of nanoparticles: Relation to heterogeneous nucleation and comparison with experiments. *J. Phys. Chem. B* **105**, 7708-7722 (2001).
41 Shchekin, A. K., Shabaev, I. V. & Rusanov, A. I. Thermodynamics of droplet formation around a soluble condensation nucleus in the atmosphere of a solvent vapor. *J. Chem. Phys.* **129**, 214111 (2008).

42 Cappa, C. D. & Wilson, K. R. Evolution of organic aerosol mass spectra upon heating: implications for OA phase and partitioning behavior. *Atmos. Chem. Phys.* **11**, 1895-1911 (2011).
43 Virtanen, A. *et al.* An amorphous solid state of biogenic secondary organic aerosol particles. *Nature* **467**, 824-827 (2010).
44 Virtanen, A. *et al.* Bounce behavior of freshly nucleated biogenic secondary organic aerosol particles. *Atmos. Chem. Phys.* **11**, 8759-8766 (2011).
45 Koop, T., Bookhold, J., Shiraiwa, M. & Poschl, U. Glass transition and phase state of organic compounds: dependency on molecular properties and implications for secondary organic aerosols in the atmosphere. *Phys. Chem. Chem. Phys.* **13**, 19238-19255 (2011).
46 Burch, D. & Bazant, M. Z. Size-Dependent Spinodal and Miscibility Gaps for Intercalation in Nanoparticles. *Nano Lett.* **9**, 3795-3800 (2009).